NANO · MICRO small
www.small-journal.com

Parallelized Mechanical Stimulation of Neuronal Calcium Through Cell-Internal Nanomagnetic Forces Provokes Lasting Shifts in the Network Activity State

*Connor L. Beck and Anja Kunze**

Neurons differentiate mechanical stimuli force and rate to elicit unique functional responses, driving the need for further tools to generate various mechanical stimuli. Here, cell-internal nanomagnetic forces (iNMF) are introduced by manipulating internalized magnetic nanoparticles with an external magnetic field across cortical neuron networks in vitro. Under iNMF, cortical neurons exhibit calcium (Ca^{2+}) influx, leading to modulation of activity observed through Ca^{2+} event rates. Inhibiting particle uptake or altering nanoparticle exposure time reduced the neuronal response to nanomagnetic forces, exposing the requirement of nanoparticle uptake to induce the Ca^{2+} response. In highly active cortical networks, iNMF robustly modulates synchronous network activity, which is lasting and repeatable. Using pharmacological blockers, it is shown that iNMF activates mechanosensitive ion channels to induce the Ca^{2+} influx. Then, in contrast to transient mechanically evoked neuronal activity, iNMF activates Ca^{2+}-activated potassium (K_{Ca}) channels to stabilize the neuronal membrane potential and induce network activity shifts. The findings reveal the potential of magnetic nanoparticle-mediated mechanical stimulation to modulate neuronal circuit dynamics, providing insights into the biophysics of neuronal computation.

1. Introduction

The brain's functionality relies not only on chemical signaling but also on mechanical cues that drive neuronal behavior.[1] Findings consistently show that neurons are sensitive to mechanical deformation of the cell membrane,[2–4] a phenomenon closely associated with transmembrane mechanosensitive (MS) ion channels.[5–7] These proteins sense and transduce mechanical stimuli to trigger a range of neuronal responses, including initiating migration[8] and polarization,[9] neurite stretching,[10–12] spine adaptations,[13–15] or tuning activity.[16,17] Neurons differentiate the magnitude and the rate of a mechanical stimulus to elicit unique functional responses.[18] While rapid and strong probing of the neuronal membrane evokes action potentials,[19,20] slow and gentle deformations alter neuronal excitability.[4,18,21] These force paradigms, observed through intracellular calcium (Ca^{2+}) imaging and electrophysiological recordings, expose a transient Ca^{2+} response to a high-force pulse stimulus,[19] whereas gentle and continuous membrane deformations induce prolonged cytosolic Ca^{2+} influx, altering excitability.[4,22] As Ca^{2+} regulates neuronal function and computation,[23] examining this slow mechanical stimulation could provide great insight into the biophysics of neuronal dynamics.

Prior work has focused on probing single neurons with a localized mechanical stimulus generated by micropipettes,[4,24,25] atomic force microscopy (AFM),[3,18] or nanotransducers.[21,26,27] These local mechanical cues can further modulate functionally coupled neighboring cells as the information propagates across the network through defined microcircuit ensembles.[4] The coordinated activity of neuronal ensembles gives rise to mechanistic functions in vitro[28] and high-order functions in vivo,[29] suggesting this mechanical information is vital to tune single neuron attributes contributing to network dynamics. Projecting this localized stimulus onto multiple neurons could provide useful insight into neuronal computation through controlling spike-timing.[30]

Parallel mechanical stimulation delivers uniform mechanical cues across neuronal networks through substrate stretching,[31,32] shear stress,[6,33,34] or ultrasound stimulation.[5,35,36] Advancements in focused ultrasound have expanded such technologies into the clinical space as non-invasive therapeutics.[37,38] However, incongruencies arise between the observed neuronal responses and associated biochemical pathways between parallelized, homogenous stimulation and localized stimulation techniques.[6] Biophysically, the pressure induced by localized forces creates high membrane curvatures, whereas homogeneous stimulation delivers uniform pressure waves of the cell.[39]

C. L. Beck, A. Kunze
Department of Electrical and Computer Engineering
Montana State University
Bozeman, MT 59717, USA
E-mail: anja.kunze@montana.edu
A. Kunze
Montana Nanotechnology Facility
Montana State University
Bozeman, MT 59717, USA
A. Kunze
Optical Technology Center
Montana State University
Bozeman, MT 59717, USA
The ORCID identification number(s) for the author(s) of this article can be found under https://doi.org/10.1002/smll.202406678

DOI: 10.1002/smll.202406678

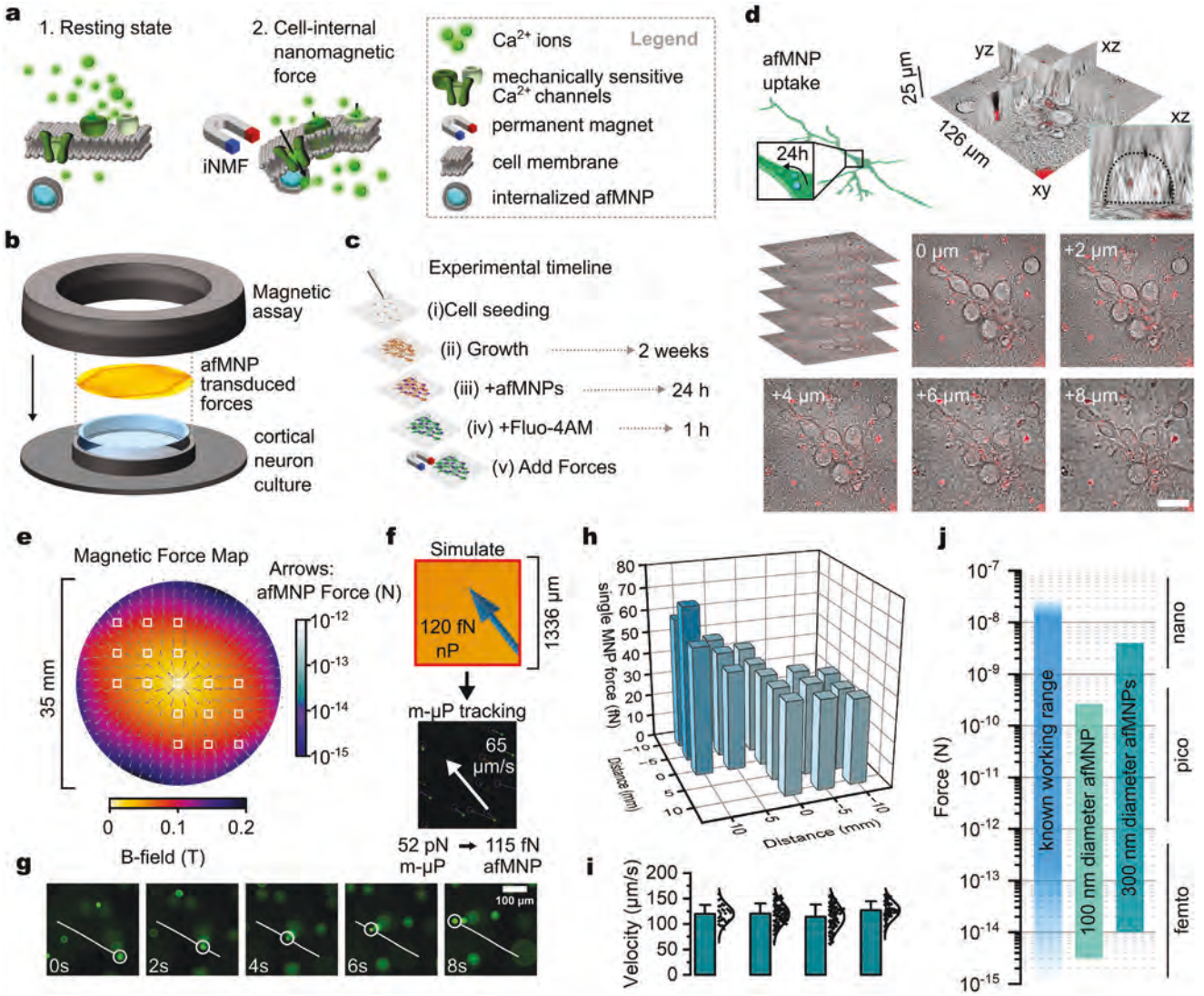

Figure 1. Precise and reproducible iNMF generation for in vitro assays. a) Mechanistic approach of intracellular-actuated Ca^{2+} influx. b) Expanded view of magnetic field assay for use with standard cell cultures. c) Experimental timeline designed to permit magnetic nanoparticle uptake in cortical networks for iNMF. d) Time and nanoparticle surface functionalization dependent neuronal uptake. 14 DIV cortical neurons exposed to afMNPs for 24 h under volumetric imaging of differential interference contrast and red fluorescence reveal internalized fluorescent afMNPs (1000x total mag, 0.18 µm z-step, oil immersion, NA 1.52). Orthogonal xz projection shows afMNPs contained in the soma of a neuron. e) Finite element modeling of the magnetic field across the dish surface and estimate afMNP cluster generated forces at a diameter of 300 nm. f) Simulated forces are validated locally with fluorescent magnetic microparticles (µP, 8.4 µm diameter) and converted to approximate magnetic nanoparticle (nP) generated forces. g) False color fluorescent image sequence of magnetic microparticle tracking h) Map of the predicted average magnetic nanoparticle gradient forces across the cell assay through magnetic microparticle tracking. i) Average velocity of particles across 4 independent trials highlights the reproducibility of forces across samples (n = 4 independent samples, >20 microparticles per sample). j) Theoretical force ranges of the magnetic nanoparticle assay contrasted against the working range. Mechanical stimulation of neurons has a known working range of ≈100 fN to ≈200 nN, where membrane rupture occurs.

The various pathways in membrane curvature sensing[40] suggest these pressure modalities trigger alternate functional responses in neurons. Therefore, we expect prioritizing slow cytosolic Ca^{2+} influx requires the delivery of local cues to impact membrane curvature.

Magnetic nanotransducers have the potential to deliver these localized forces throughout neuronal networks. A magnetic nanotransducer converts the electromagnetic energy of an external magnetic field to generate localized forces across neuronal networks.[2,21,22] Specifically, magnetic nanotransducers produce mechanical interactions on the environment through torque driven by transitions in the magnetization state[2] or force driven by the magnetic gradient.[41] Torque-generating magnetic nanodiscs can modulate neurons through mechanical[42,43] and thermal[44–46] means with rapid temporal precision. The use of magnetic coils enables magnetic nanotransducer interactions in complex in vivo settings to modulate behavior[47–50] or serve as a therapeutic.[51] Permanent magnetic field manipulation of magnetic nanoparticles, deemed nanomagnetic forces, is essential for isolating mechanical stimulation from

magnetothermal generation.[52] With permanent magnetic fields, magnetic nanoparticles adhered to the neuronal membrane require force amplification from magnetically permeable substrates to manipulate the magnetic gradient and achieve sufficient nanomagnetic forces to induce Ca^{2+} influx.[53,54] These substrates restrict the nanomagnetic forces to small areas with heterogenous forces,[21] thus mitigating the potential for broad network stimulation. However, recent findings demonstrated that nanomagnetic forces without force amplification induce a functional impact on neurons using cell-internalized magnetic nanoparticles.[55] As magnetic nanoparticle internalization gives access to the cytosol, forces are exerted on the cell membrane and through cytoskeletal interactions. It remains unclear if these cytosolic-localized magnetic nanoparticle forces can induce Ca^{2+} influx or create lasting impacts on the network. Moreover, the mechanism of force generation through cytoskeletal forces remains unclear.

Here, we describe a platform for the large-scale, remote magnetic manipulation of neuron-internalized magnetic nanoparticles to deliver cell-internal nanomagnetic forces (iNMF) across in vitro cortical networks. Through fluorescent imaging, we show that iNMF induces Ca^{2+} influx and modulates the Ca^{2+} event rate in cortical neuronal networks. We find particle internalization is required to observe Ca^{2+} influx during force generation, hinting at neuronal differentiation of cell-internal and external forces. Then, we uncover a lasting and repeatable shift in network activity during iNMF on dense cortical networks, highlighted by a dysregulation in network synchrony. Through pharmacological inhibition, we find that MS channels mediate Ca^{2+} influx during iNMF and Ca^{2+}-activated potassium channels stabilize the membrane potential and drive these observed network shifts. These results provide a framework for parallelized local mechanical stimulation of cortical networks, expanding insights into the biophysics of neuronal computation.

2. Results

2.1. Reproducible Mechanical Force Generation With iNMF

To study iNMF on cortical networks in vitro, we developed a magnetic assay consisting of permanent rare-earth magnets (N52) to generate magnetic force gradients on magnetic nanoparticle-laden cortical networks in standard 35 mm Petri dish assays (**Figure 1a–c**). Cortical neurons are known to internalize magnetic nanoparticles,[56,57] with amine surface functionalization enhancing the likelihood of cell uptake.[58,59] Therefore, we utilized the physiochemical properties of the magnetic nanoparticle surface to enhance the uptake of magnetic nanoparticles, prioritizing force generation within the intracellular space.[60] Amine-functionalized, 100 nm starch bionized nanoferrite fluorescent magnetic nanoparticles (afMNPs) were incubated with 13 DIV primary rat cortical neurons (E18) for 24 h following previous particle uptake methods.[61] High resolution, volumetric differential interference contrast (DIC), and red fluorescent particle co-imaging confirmed particle uptake after 24 h afMNP exposure (Figure 1d). The afMNPs were predominantly associated with the cytosol and neurites. However, observations could not exclude the possible co-existence of surface-bound particles on the cortical networks.

Finite element modeling of magnetic fields and force estimations[54] of the magnetic nanoparticles presented a range of magnetic gradient forces (0.1–16 $kg^2m^{-1}s^{-4}A^{-2}$) across a standard culture dish (Figure 1e; Figures S1–S3, Supporting Information). The forces remained homogenous within local (1.3 mm^2) fields of view (Figure 1f). We tested the uniformity and consistency of force generation within imaging windows through magnetic particle image velocimetry (Figure 1g). Tracked magnetically susceptible fluorescent microbeads moved at a constant velocity (8.4 µm, suspended in PBS), indicating equivalency of microparticle and drag forces (Figure S4, Supporting Information). We observed limited variability in estimated magnetic nanoparticle forces estimations across the assay (Figure 1h). Repeated uses of the magnetic assay exhibited no significant variance in microparticle velocity within the same field of view, highlighting the cross-sample reproducibility (Figure 1i). Through finite element modeling and particle tracking estimations, we predict single nanoparticles in the assay produce a maximum magnetic gradient force of 10 fN, below any known force sensitization.[62] We suspect an aggregative magnetic nanoparticle effect is essential to generate forces (Figures S1–S3, Supporting Information). Accounting for magnetic nanoparticle clustering (maximum 300 nm diameter) and local cytoskeletal interactions, afMNPs across the assay exert a range of 2 fN to 3nN on a single neuron (Figure 1j; Figure S2, Supporting Information).

2.2. iNMF Modulates Cortical Neuron Ca^{2+} Dynamics

To identify the impacts of iNMF stimulation, we cultured rat primary cortical neurons (E18) to 13 DIV to form functional networks. Immunofluorescent staining showed various excitatory and inhibitory neurons present in culture with astrocytes (Figure S5, Supporting Information). We exposed the cortical networks to afMNPs for 24 h to encourage cell uptake before gentle cell wash to remove excess particles. Under stage-top incubation, fluorescent imaging of Ca^{2+} dynamics (Fluo-4AM, 4 Hz) performed in consecutive (4 min) phases (baseline, modulation, and recovery) allowed for continual tracking of individual cells over the experimental phases (**Figure 2a**). Somatic Ca^{2+} influx increased significantly in afMNP-laden cortical cells during the iNMF modulation phase (Figure 2b; Video S1, Supporting Information). A minor fluorescent decay under the baseline period, independent of nanoparticle interactions, suggested photobleaching occurred under imaging (Figure S5, Supporting Information). We decomposed individual somatic fluorescent traces into a resting Ca^{2+} waveform that excludes short-term influx events to estimate the lower bounds of Ca^{2+} during iNMF-driven influx and detect transient Ca^{2+} influx events to approximate activity (Figure 2c; Figures S6 and S7, Supporting Information). Cumulative Ca^{2+}, measured as the area under the resting Ca^{2+} waveform, approximated the magnitude of Ca^{2+} flux (Figure 2d). To quantify the observed decrease in Ca^{2+} event activity, we extracted a Ca^{2+} event rate by binning Ca^{2+} events over each minute of imaging (Figure 2e). Unlike the short-term, transient Ca^{2+} responses to rapid mechanical indentation,[18] the slow influx of cytosolic

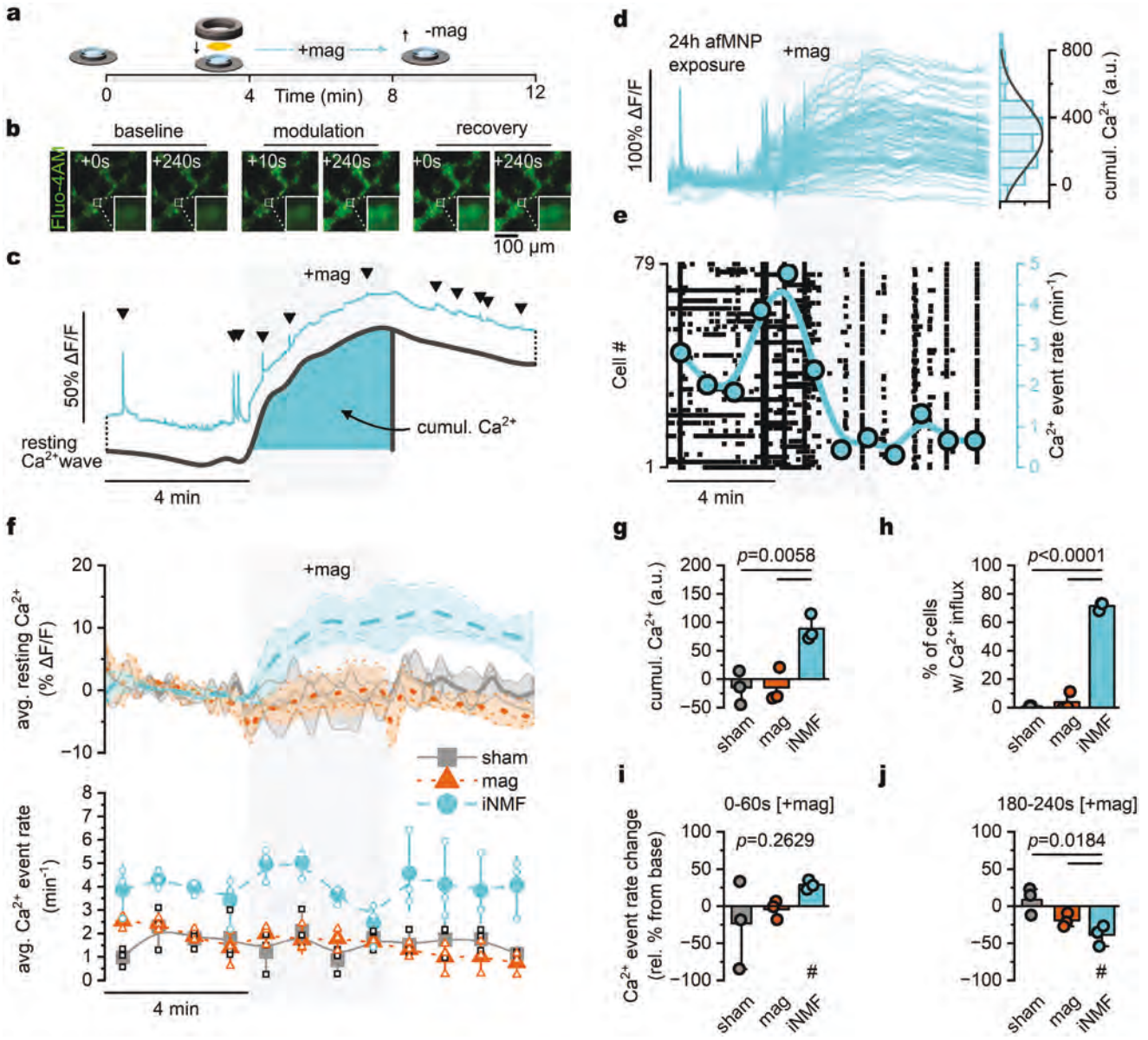

Figure 2. iNMF induced Ca^{2+} influx and reduced event activity. a) Experimental protocol for remote iNMF on cortical neurons. b) Representative time-lapse images of Fluo4-AM before (baseline), during (modulation), and after (recovery) iNMF. c) Average Fluo-4AM somatic ΔF/F signal of example neuron (blue trace) is decomposed into a resting Ca^{2+} wave (black trace) and transient activity as Ca^{2+} events (black triangles). d) Representative ΔF/F waveforms of a 14 DIV cortical neuron network (n = 79 cells) response to iNMF highlights the influx of somatic Ca^{2+} and quantified by a histogram of individual cell cumulative Ca^{2+} during +mag. e) Ca^{2+} event raster plot corresponding to the traces in (d) exhibit reduced Ca^{2+} event activity during iNMF and lasted following the removal of the magnetic field. Overlaid blue circles is the average Ca^{2+} event rate measured in 1 min windows with b-spline line connection. f) Resting Ca^{2+} and Ca^{2+} event responses of large (>500 cells/mm2) cortical neuron networks to iNMF. Bold lines and shaded region or vertical bars are mean ± SD. Thin lines and open shapes are individual sample observations (n = 3 independent experiments per group; sham: no afMNPs + no mag device, mag: no afMNPs + mag device, iNMF: with afMNPs + mag device). g) Average cumulative Ca^{2+} flux of each network recorded and h) relative % of cells exhibiting peak resting Ca^{2+} (>5% ΔF/F). i,j) Change in Ca^{2+} event activity during the (i) first and (j) final min of modulation. The data in (g–j) are mean ± SD of n = 3 independent experiments plotted in (f) where p-values are 1-way ANOVA and post-hoc Tukey test with $p < 0.05$ represented as solid lines. Significant deviations from baseline activity in (i,j) were found with two-tailed paired t-tests of the activity rate across the corresponding minute against the average activity rate during baseline (not shown p>0.05, # $p < 0.05$).

Ca^{2+} suggests cortical neurons sense iNMF as a slow, local force stimulus.

Next, large populations of cortical neurons (>500 cells mm^{-2}, DIV 13) were exposed to afMNPs for 24 h, and contrasted against no nanoparticle controls (Figure 2f). Following observations from previous magnetic nanoparticle interactions with neurons,[22,63] the afMNPs induced greater spontaneous Ca^{2+} event rates (3.9 ± 0.37 min^{-1}) than non-exposed cells (1.7 ± 0.54 min^{-1}). The afMNPs did not induce a significant change in the temporal variance on the Ca^{2+} event rates during the baseline period

(Figure S8, Supporting Information), indicating that the neuronal network activity was stabilized by 24 h afMNP exposure. Under the addition of the magnetic field, afMNP-laden cultures presented significant network-wide Ca^{2+} influx with an average cumulative Ca^{2+} influx of 89 ± 23 a.u. where ≈71 ± 2.9% of neurons responded (peak influx greater than 5% ΔF/F). Neither the application of a sham device nor magnetic field device without afMNPs showed significant Ca^{2+} influx with −15 ± 30 a.u. and −14 ± 30 a.u. cumulative Ca^{2+} influx respectively (Figure 2g,h). Combined with the observed resting Ca^{2+} influx in the neurons, there was a significant modulatory response in the Ca^{2+} event rate. Over the first minute of stimulation, we observed a significant increase in the Ca^{2+} event rate to 5.0 ± 0.70 min^{-1} (Figure 2i), followed by repression in activity by the fourth minute of applied iNMF to 2.5 ± 0.91 min^{-1} (Figure 2j) and inconsistent activity profiles during the recovery period. Neither magnetic field, nor sham experiments exhibited this Ca^{2+} event rate shift, specifying afMNP-mediated stimulation.

The prolonged somatic Ca^{2+} observed following the removal of the magnetic field did not return to baseline intensity within the recording window, so we extended recordings following iNMF exposure (Figure S9, Supporting Information). Cytosolic Ca^{2+} returned to baseline following 5 min of rest. However, the event activity remained significantly reduced for at least 20 min. Given the relationship of Ca^{2+}, neuronal activity, and cell death,[64,65] we suspected these forces could play a role in the viability of cells. We performed live-dead staining following iNMF with BOBO-3 iodide to detect loss of membrane integrity (Figure S10, Supporting Information). There was no significant increase in cell death or membrane integrity loss in iNMF exposed samples, so we then probed the relationship between Ca^{2+} and reactive oxygen species (ROS) generation through fluorescent imaging the following day (Figure S11, Supporting Information). ROS intensity was significantly decreased in cells exposed to afMNPs, and further decreased by cells exposed to iNMF, suggesting reduced ROS expression.

2.3. Neuronal Uptake of afMNPs is Necessary for Ca^{2+} Influx During iNMF

Next, we aimed to characterize the relationship of afMNP uptake to the iNMF response. Neuronal uptake mechanisms for particles at or above 100 nm are limited to macropinocytosis, phagocytosis, and clathrin-mediated endocytosis.[66] We pharmacologically inhibited these mechanisms during afMNP exposure by depolymerization of the F-actin cytoskeleton[67,68] through cytochalasin D (CytD, 1 μM) exposure, and performed Pitstop 2 (PIT2, 20 μM) specific inhibition of clathrin-mediated endocytosis[69] (**Figure 3a**). Pharmacological agents were added to 13 DIV cortical neurons 30 min prior to the addition of afMNPs. After 24 h co-exposure of blocker/afMNPs, we removed excess particles and pharmacological agents from the cells by gently washing them. The cultures underwent a 2.5 h incubation following the wash to ensure the actin cytoskeleton in CytD exposed cultures was re-stabilized.[67,68,70] High-resolution imaging (1000x total magnification, oil immersion, NA 1.52) with DIC and red fluorescent afMNP imaging enabled particle uptake identification. Cultures exposed to PIT2 and afMNPs showed similar uptake as those exposed to DMSO controls, while neurons exposed to CytD minimized, but did not abolish, afMNP uptake (Figure 3b; Figure S12, Supporting Information).

To test whether the mitigation of afMNP uptake altered the Ca^{2+} influx response, we performed Ca^{2+} imaging on cultures following co-exposure of the uptake inhibitors with afMNPs. Under the magnetic field exposure, PIT2/afMNP co-exposed cultures exhibited no significant difference in Ca^{2+} influx (89.1 ± 11.3 a.u.) from no inhibitor DMSO/afMNP exposed controls (76.3 ± 12.2 a.u.) (Figure 3c). However, cultures co-exposed with CytD/afMNPs exhibited significantly less Ca^{2+} influx (−1.6 ± 11.9 a.u.) than that of no inhibitor DMSO/afMNP controls (54.4 ± 16.4 a.u.), indicating afMNP uptake is necessary to observe Ca^{2+} influx with the large-scale platform.

Based on these results, we altered the magnetic field pull direction during iNMF to pull downward into the dish surface in contrast to the previous vertical pulling. Biophysically, external membrane-bound particles induce membrane forces independent of direction, while only vertical forces generated by internalized particles can deform the unconstrained membrane. The downward pulling of afMNPs significantly reduced the magnitude of Ca^{2+} influx compared to the vertical pull direction (Figure S13, Supporting Information). Therefore, we use the vertical pull direction for all other experiments in this work. These observations suggest that the neurons respond specifically to cell-internal forces during iNMF.

2.4. Magnetic Nanoparticle-Neuron Interactions Influence Ca^{2+} Response to iNMF

Next, we leveraged the dependency of neuronal uptake on nanoparticle surface chemistry and exposure timing to test for differences in the Ca^{2+} response during nanomagnetic forces. Nanoparticle uptake is a time and energy-dependent process,[66] mediated through particle surface chemistry and charge.[60,71] To examine the time-dependency across nanoparticle – neuron interactions, we selected plain starch functionalized bionized nanoferrite particles[22,57] and magnetite (neutral or anionic) magnetic nanoparticles. Following sonication (37 kHz, 30 min, 40 °C), zeta-potential measurements through dynamic light scattering (DLS) of nanoparticles in culture media presented a neutral surface charge in all particles except the anionic particles, which exhibited a slight negative surface charge of −15.5 ± 2.8 mV (**Figure 4a,b**). DLS measurements did not present nanoparticle clustering for the afMNPs with a radius of 63 ± 27 nm and the starch-functionalized magnetic nanoparticles with a radius of 49 ± 9 nm (Figure S14, Supporting Information). However, magnetite nanoparticles clustered with a 341 ± 81 nm radius for neutral and a 771 ± 232 nm radius for anionic magnetic nanoparticles in media. All particles presented a polydispersity index below 0.2, indicating the nanoparticles were monodisperse.

Cultured neurons underwent exposure to magnetic nanoparticles for 4 or 24 h, allowing Ca^{2+} recordings on 14 DIV. Under magnetic field exposure, the afMNPs showed no significant exposure time dependency, with 66 ± 36% cells responding after 4 h exposure, while 62 ± 10% of 24 h exposed cells responded (Figure 4c1–e1). The considerable variability at 4 h suggests cortical neurons uptake the afMNPs around 4 h. Plain

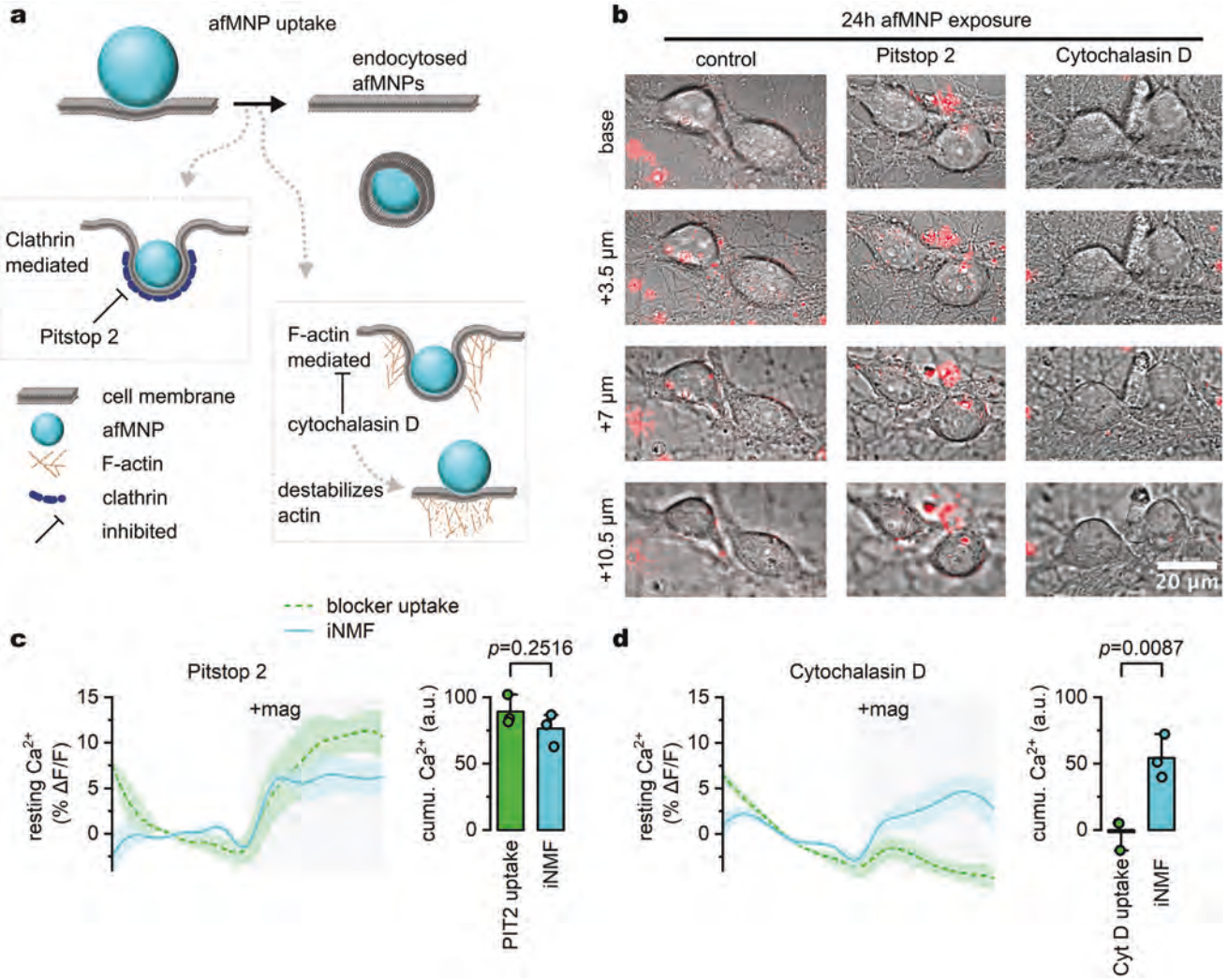

Figure 3. afMNP uptake mediates iNMF induced Ca^{2+} influx a) Schematic of afMNP uptake mechanisms tested. b) Representative volumetric phase contrast and red fluorescent imaging of cortical neurons after 24 h co-exposure with afMNPs and pharmacological inhibition of clathrin-mediated endocytosis, Pitstop 2 or actin-mediated uptake inhibition with Cytochalasin D (1000x total magnification, oil immersion NA 1.52). Cultures were treated with uptake inhibitors for 30 min prior to afMNP exposure with control cells receiving DMSO treatment. c) Pitstop 2 inhibition during afMNP co-exposure (PIT2 uptake) showed no reduction in the Ca^{2+} influx response of cultures compared to standard afMNP exposure (iNMF). Data is plotted as mean ± SD (n = 3 independent experiments; unpaired two-tailed t-test with equal variance). d) Ca^{2+} influx response of cultures exposed to Cytochalasin D was significantly reduced against standard afMNP exposure. Following 24 h co-exposure with Cytochalasin D, cells were washed and provided 2.5 h incubation to restabilize the actin cytoskeleton. Data in (c,d) is plotted as mean ± SD (n = 3 independent experiments each, unpaired two-tailed t-test with equal variance).

starch magnetic nanoparticles contrasted the incubation time independency with significantly greater responding cells to nanomagnetic forces at 24 h exposure (86 ± 20%) in contrast to 4 h exposure (16 ± 18%) with a similar significance on Ca^{2+} influx magnitude (Figure 4c2–e2). Given that starch magnetic nanoparticles remain extracellular at 4 h exposure in cortical neurons,[22] this evidence suggests that particle internalization is necessary to observe responses to nanomagnetic force induced by this magnetic assay. Neurons responded to anionic charged magnetite nanoparticle mediated nanomagnetic force with 20 ± 42% of cells responding for 4 h exposure and 70 ± 40% cells responding for 24 h exposure (Figure 4c3–e3) while neutral magnetite nanoparticle exposed cultures minimally responded to the nanomagnetic forces, with 9 ± 12% of cells responding at 4 h exposure and 33 ± 30% of cells responding at 24 h exposure (Figure 4c4–e4). The temporal response across various nanoparticle surface chemistries furthers the hypothesis that the neuromodulatory response of nanoparticle-mediated forces is dependent on the nanoparticle-neuron interaction.

2.5. iNMF Robustly Shifts Neuronal Network Synchrony

Having established that iNMF induces Ca^{2+} influx in neurons and modulates the Ca^{2+} event rates, we aimed to further probe the relationship between iNMF and network activity. The cumulative

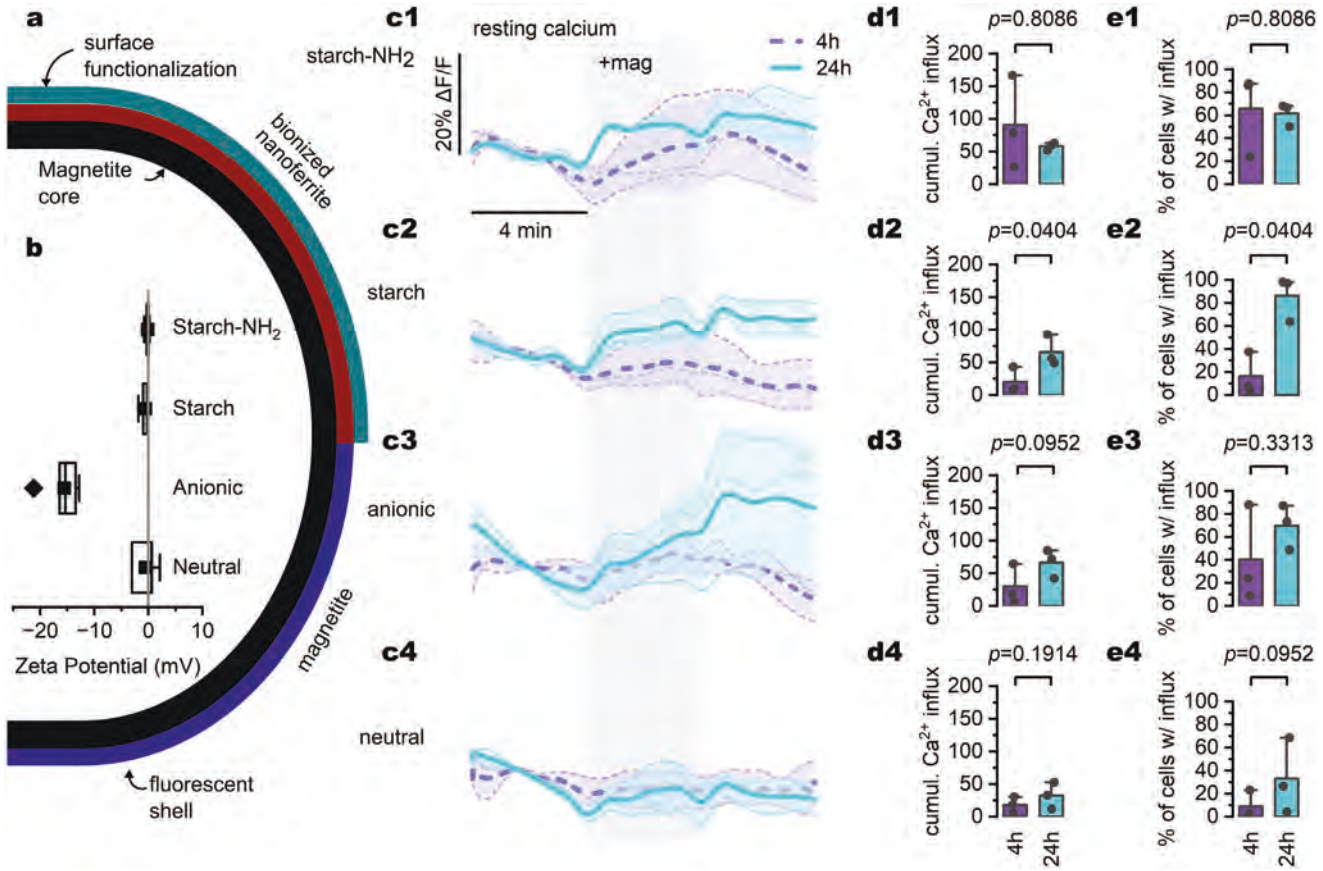

Figure 4. Ca^{2+} influx response to iNMF dependent on magnetic nanoparticle interactions. a) Schematic of magnetic nanoparticle structure. b) Zeta potential measurements for the nanoparticles measured in PBS. c) Resting Ca^{2+} measurements of 14 DIV cortical neurons during iNMF with differing magnetic nanoparticle surface chemistry (**1** starch-NH_2 **2** starch **3** anionic and **4** neutral) and exposure (4 h: dashed purple lines or 24 h: solid blue lines, bold lines and shaded regions are mean±SD while thin lines are individual sample observations). d) Exposure time differential response of the average cumulative Ca^{2+} influx and e Relative % of cells exhibiting peak resting Ca^{2+} (>5% ΔF/F). Statistical analysis in (d,e) is single-tailed, Mann-Whitney test (n = 3 independent samples each, $\mu_{4\,h} < \mu_{24\,h}$).

Ca^{2+} response to iNMF was significantly reduced in cultures with low average Ca^{2+} event activity (1.25 ± 1.93 min^{-1}) in contrast to cultures with strong activity (4.18 ± 4.50 min^{-1}) during the baseline window (Figure S15, Supporting Information). These results suggest that the Ca^{2+} modulation is dependent on the neuronal network activity. Dense neuronal networks are known to exhibit increased frequency of neuronal transient event rates[72] and increased synchrony across the network.[73] Therefore, we aimed to test the potential of iNMF by modulating highly active, dense (>1000 cells mm^{-2}) cortical networks with iNMF (**Figure 5a**). Following 24 h afMNP exposure, dense cultures exhibited high spontaneous Ca^{2+} event activity with an average Ca^{2+} event rate of 6.3 ± 1.9 min^{-1} and extensive network synchrony. Under iNMF, the dense networks presented a significant reduction in Ca^{2+} event activity (Figure 5b), characterized by a lack of synchronous network events (Figure 5c; Video S2, Supporting Information). Sørenson-Dice correlation (SD) synchrony measures along Ca^{2+} event trains revealed the synchronous decrease occurred over the second min, correlated to the saturation point of Ca^{2+} influx (Figure 5d). To clarify the modulation on synchronous activity; we decomposed the Ca^{2+} event rate into synchronous (>10% of the population exhibiting a Ca^{2+} event within the 250 ms) and asynchronous (remaining Ca^{2+} events) activity rates (Figure 5e). iNMF not only suppressed synchronous Ca^{2+} event activity but also amplified asynchronous activity (Figure 5f). By min 4 of iNMF, synchronous activity reduced significantly by 100% (relative percent difference to synchronous baseline). In contrast, asynchronous activity significantly increased by 25% (relative percent difference to asynchronous baseline) (Figure 5g).

2.6. iNMF Shifted Neuronal Network Dynamics are Lasting and Repeatable

To better understand iNMF modulation of network synchrony, we probed the dense cortical networks with repeated iNMF. As the network synchrony remained suppressed following the recovery period, we hypothesized that iNMF induces a lasting alteration in the network dynamics (**Figure 6a**). Under stage top incubation, fluorescent imaging of Ca^{2+} dynamics (Fluo-4AM, 4 Hz) followed the previous methods with baseline (b), modulation (iNMF), and recovery (r). We delayed the recovery recording for 5 min to permit cytosolic Ca^{2+} re-stabilization. After recording the network's recovery, a 15-min incubation pause allowed

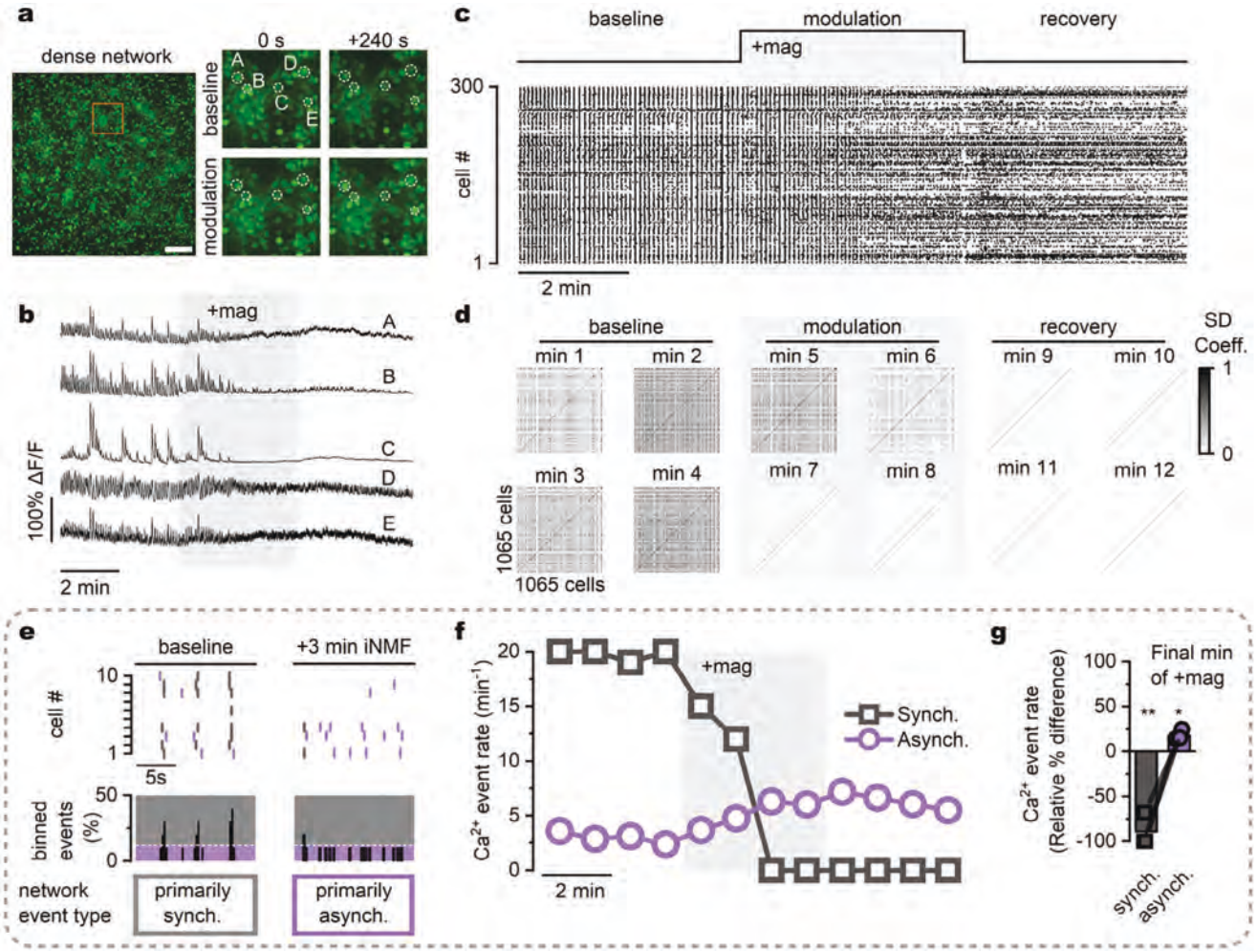

Figure 5. iNMF on dense cortical networks dysregulates network synchrony. a) False color fluorescent images of a high-density 14 DIV cortical network with 24 h afMNP exposure and Fluo-4AM labeled (scalebar: 200 µm). b) Fluorescent Ca^{2+} traces of neurons highlighted in (a) show suppression of activity during iNMF. c) Raster plot of the high activity cortical network shows a dysregulation of Ca^{2+} event activity following 4 min of iNMF. d) Sorenson–Dice correlation matrices of the total population were mapped from cell-paired event trains before (baseline), during (modulation), and after (recovery) iNMF (1 indicates high synchronous correlation). e) Decomposition of synchronous and asynchronous activity. Synchronous events are defined as >10% of the total population exhibiting a Ca^{2+} event in a 250 ms window. f) Average Ca^{2+} event rates decomposed into synchronous and asynchronous events highlight the switch between synchrony and asynchrony (n = 1065 cells from single network). g) Arresting of synchronous activity and simultaneous amplification of asynchronous activity found by contrasting decomposed average baseline activity to the fourth min of iNMF (n = 3 independent samples, one sample t-test, h_0: $\mu = 0$ h_a: $\mu \neq 0$, synchronous: $p = 0.0070$, asynchronous: $p = 0.0155$).

for extended neuronal recovery before we repeated the stimulation protocol to investigate the recursive properties of iNMF stimulation.

We observed repeatable Ca^{2+} influx and synchronous network modulation, with partial recovery of synchrony during both recovery phases (Figure 6b). Synchronous and asynchronous Ca^{2+} event rates projected the network dynamics into a latent state space at 60s intervals to allow for smooth state transitions (Figure S16, Supporting Information). The latent distance from the current state to the initial state (Δstate) enabled the mapping of state transitions (Figure 6c). Cortical networks exposed to afMNPs but not to magnetic fields resided in a consistent state with a variance of 4.0 ± 2.5 min^{-1} over multiple hours (Figure S17, Supporting Information). During iNMF, networks deviated from the baseline state (b1) with a Δstate of 8.2 ± 2.8 min^{-1} and partial recovery of the Δstate following 5 min rest to a Δstate of 4.3 ± 1.8 min^{-1} during the first recovery period (Figure 6d,e). A 15 min incubation period had little effect on reducing the Δstate, with a value of 3.6 ± 2.1 min^{-1}. Repeating iNMF returned the network to a similar state space as the first stimulation with a Δstate of 8.5 ± 3.6 min^{-1} and a secondary recovery Δstate of 6.8 ± 1.8 min^{-1} showing the lasting deviation from the baseline.

To test if inhibitory cues mediated the alterations of the network state, we introduced 50 µM bicuculline, a selective antagonist of gamma-aminobutyric acid type a ($GABA_A$) receptors after the first phase of iNMF to chemically suppress inhibitory inputs (Video S3, Supporting Information). Bicuculline was added immediately following r1, providing exposure for 15 min before recording in b2. Under bicuculline exposure, the network

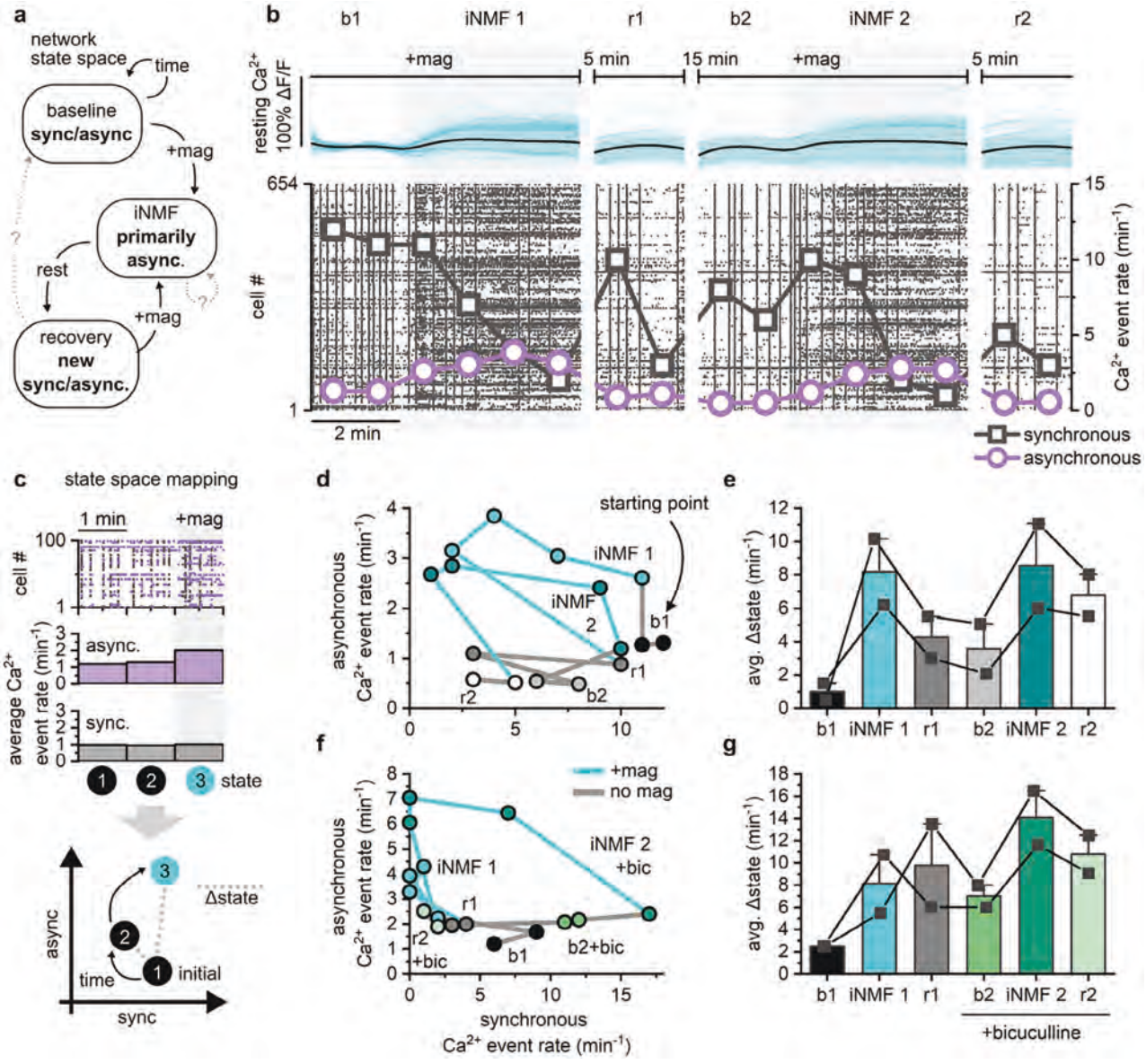

Figure 6. Synchronous network finds new state following iNMF. a) Network state diagram with observed network behaviors under iNMF in solid black lines and possible state transitions of interest as dotted gray lines. b) Resting Ca^{2+} signals and corresponding raster plot with overlaid synchronous (>10% of the population exhibiting Ca^{2+} event in 250 ms) and asynchronous (remaining Ca^{2+} events) activity for 24 h afMNP exposed cortical networks (DIV 14) exposed to iNMF twice with resting periods. Surrounding iNMF stimulation, baseline (b) and recovery (r) activity rates were recorded to map the response. c) Network states, defined here as the balance between synchronous and asynchronous activity are extracted from synchronous and asynchronous decomposed Ca^{2+} event rates. The relationship between asynchronous and synchronous activity is mapped to a state space, with the change of state (Δstate) measured by the mean square distance relative to the initial state. d) Representative network state from the activity profile plotted in (b) shows similar time-dependent network state response during both iNMF stimulations with new network states arising in r1 and r2. e) Average Δstate during each phase (iNMF phases is averaged over min 3–4) shows the divergence in state space from the initial following iNMF. (n = 2 independent experiments). f) Pharmacological inhibition of GABA-A receptors with bicuculline (50 μM) following an initial iNMF stimulation presented over-recovery of synchronous activity following 15 min exposure in b2 and rapid silencing of synchronous events during repeated iNMF stimulation. g) Average Δstate during each phase exposed the shift in activity during iNMF + bicuculline and the inability to recover activity (n = 2 independent experiments each).

exhibited elevated activity, primarily in synchrony (Figure 6f,g). The pharmacological state stabilized beyond the networks initial position to Δstate of 7.0 ± 1.4 min^{-1}. Application of iNMF while still under bicuculline exposure significantly altered the network dynamics, with a Δstate of 14.1 ± 3.4 min^{-1}, indicating that iNMF outruns the excitatory network tone of bicuculline. Following a 5 min rest, the bicuculline could not return activity for the second recovery, with the Δstate (10.8 ± 2.4 min^{-1}) remaining further than the previous recovery. These results confirm that cortical networks adjust their activity state following iNMF and suggest

that iNMF forms a lasting impact on the computation of these circuits.

2.7. iNMF Activates Mechanosensitive ion Channels and Downstream Ca^{2+}-Activated Potassium Channels

To elucidate the relationship between iNMF and network activity, we characterized the biochemical mechanisms by independently inhibiting key neuronal features associated with mechanical sensitivity and Ca^{2+} flux. We introduced pharmacological blockers of candidate channels and receptors to afMNP-laden cultures (14 DIV) for 20 min before Ca^{2+} imaging (**Figure 7a**). We decomposed the characterization of blocker interactions into Ca^{2+} influx and modulation of activity. Under iNMF, we use only the asynchronous response, as the initial synchronous activity rate varied across pharmacological agents. Because iNMF created lasting impacts on the network, we used independent no-blocker DMSO controls to contrast against. Under iNMF the DMSO controls exhibited a cumulative Ca^{2+} of 76 ± 13 a.u. and a 43 ± 19.8% change in asynchronous activity relative to the average baseline activity matching our previous observations.

To determine if MS channels mediated Ca^{2+} entry, we exposed gadolinium chloride (Gd^{3+}, 50 µM) as a non-specific blocker of MS channels through membrane packing.[74] In the presence of Gd^{3+}, the cumulative Ca^{2+} (33 ± 13 a.u.) and asynchronous event rate percent change of 4 ± 3% from baseline activity under iNMF was significantly lower than controls, confirming the role of MS channels in iNMF (Figure 7c). The partial Ca^{2+} influx under Gd^{3+} may be due to the low concentration or partial removal of Gd^{3+} by the magnetic field.[75,76] As Gd^{3+} inhibits voltage-gated Ca^{2+} channels,[77,78] we used selective blockers ω-conotoxin GIVA (CTX, 100 nM) and ω-agatoxin IVA (AGA, 100 nM) to inhibit N-type and P/Q-type voltage-gated Ca^{2+} channels respectively. Neurons treated with either voltage-gated Ca^{2+} channel blocker showed no significant reduction in cumulative Ca^{2+} influx or asynchronous activity under iNMF (Figure 7d,e). These results suggest that voltage-gated Ca^{2+} channels are not involved with the low forces of iNMF.

Next, we aimed to investigate the interplay between iNMF and intracellular Ca^{2+} stores. Intracellular Ca^{2+} stores, namely the endoplasmic reticulum, are depleted under significant cellular deformation.[79,80] This depletion, demonstrated in traumatic[81] and sub-threshold[82] forces, was further correlated to increased cytosolic Ca^{2+}. We inhibited the sarco/endoplasmic reticulum (SERCA) ATPase with Cyclopiazonic Acid (CPA, 4 µM) to first deplete the stores of Ca^{2+}. Under iNMF, there was no significant difference in Ca^{2+} influx from CPA-exposed cultures compared to DMSO controls. However, there was inconclusive evidence of an increased asynchronous activity response (150 ± 135% change) with a multiphase synchronous suppression in the 2 of the CPA samples (Figure 7f; Figure S18, Supporting Information), suggesting intracellular Ca^{2+} stores might play a role in the stabilization of activity following iNMF.

Finally, we hypothesized that increasing cytosolic Ca^{2+} through iNMF creates a feedback loop with Ca^{2+}-activated potassium channels (K_{Ca}), causing a shift in activity. The application of apamin (APA, 100 nM), a blocker of large conductance potassium channels, significantly suppressed the cumulative Ca^{2+} influx (43 ± 12 a.u.) but showed no mitigation of asynchronous activity increases during iNMF (Figure 7g). Inhibition of small conductance (SK) channels with paxilline (PAX, 40 nM) showed no significant suppression of Ca^{2+} influx or activity (Figure 7h). We observed one sample within the PAX group that presented with a negative cumulative Ca^{2+} (−23.9 a.u.), which occurred within the variance of sham samples (−14.5 ± 29.5 a.u.). The application of TRAM34 (400 nM), a blocker of intermediate conductance (IK) K_{Ca} channels, significantly suppressed both the influx of Ca^{2+} and asynchronous activity (Figure 7i), signifying that the overactivation of IK channels by Ca^{2+} is involved in the network dysregulation.

3. Discussion

The results of this study provide a reliable and large-scale approach to generating parallelized local force stimulation of cortical networks in vitro through iNMF. We show that continuous iNMF on the minute timescale provokes a sustained influx of cytosolic Ca^{2+} paired with a modulatory impact on Ca^{2+} events. Unlike transient Ca^{2+} responses to short pulses generated by AFM[6,18] and ultrasound stimulation,[5,36] the continuous influx of somatic Ca^{2+} under iNMF furthers the hypothesis that neurons differentiate both the rate and magnitude of mechanical probing. The stimulation was dependent on afMNP uptake, which could indicate that neurons either differentiate cell-internal and cell-external forces or that an aggregative effect provided by internalization was required to generate sufficient force. By limiting the time-dependent uptake of magnetic nanoparticles of differing surface chemistry, we find further evidence that particle internalization rather than membrane association consistently induces sustained Ca^{2+} influx. Our results indicate that the actin cytoskeleton influences afMNP uptake. Amine functionalization of nanoparticles is recognized for enhancing cellular uptake.[61,83,84] The mechanisms associated with amine-functionalized nanoparticles include clathrin-mediated endocytosis and lipid-raft endocytosis.[85] In our study, we found that afMNPs remained present following pharmacological inhibition of clathrin-mediated endocytosis. This could indicate that lipid-raft endocytosis or non-receptor-mediated endocytosis mechanisms such as micropinocytosis or phagocytosis mediate the uptake. As nanoparticle uptake can occur through multiple mechanisms, it is possible that clathrin-mediated endocytosis occurs in parallel with other endocytic mechanisms during non-inhibited exposure. Future work should prioritize the specific characterization of the endocytic mechanisms involved. The mechanism of endocytosis defines the fate of nanoparticles within the cell,[86] providing insight into the long-term stability of nanoparticles for in vivo studies.[87]

There was no reduction in cell viability after 24 h afMNP exposure or iNMF, indicating that the neuronal response was not due to nanotoxicity. When internalized, iron oxide particles facilitate redox cycling via the Fenton reaction, enhancing ROS production and contributing to cytotoxicity.[88,89] Several factors, including size and coating contribute to particle oxidation. A reduction in particle radius increases the surface area-to-volume ratio, permitting increased oxidation due to a greater reaction interface. Our nanoparticles, ≈100 nm in diameter, should exhibit lower cytotoxicity compared to smaller (< 20 nm) iron oxide particles.[90,91]

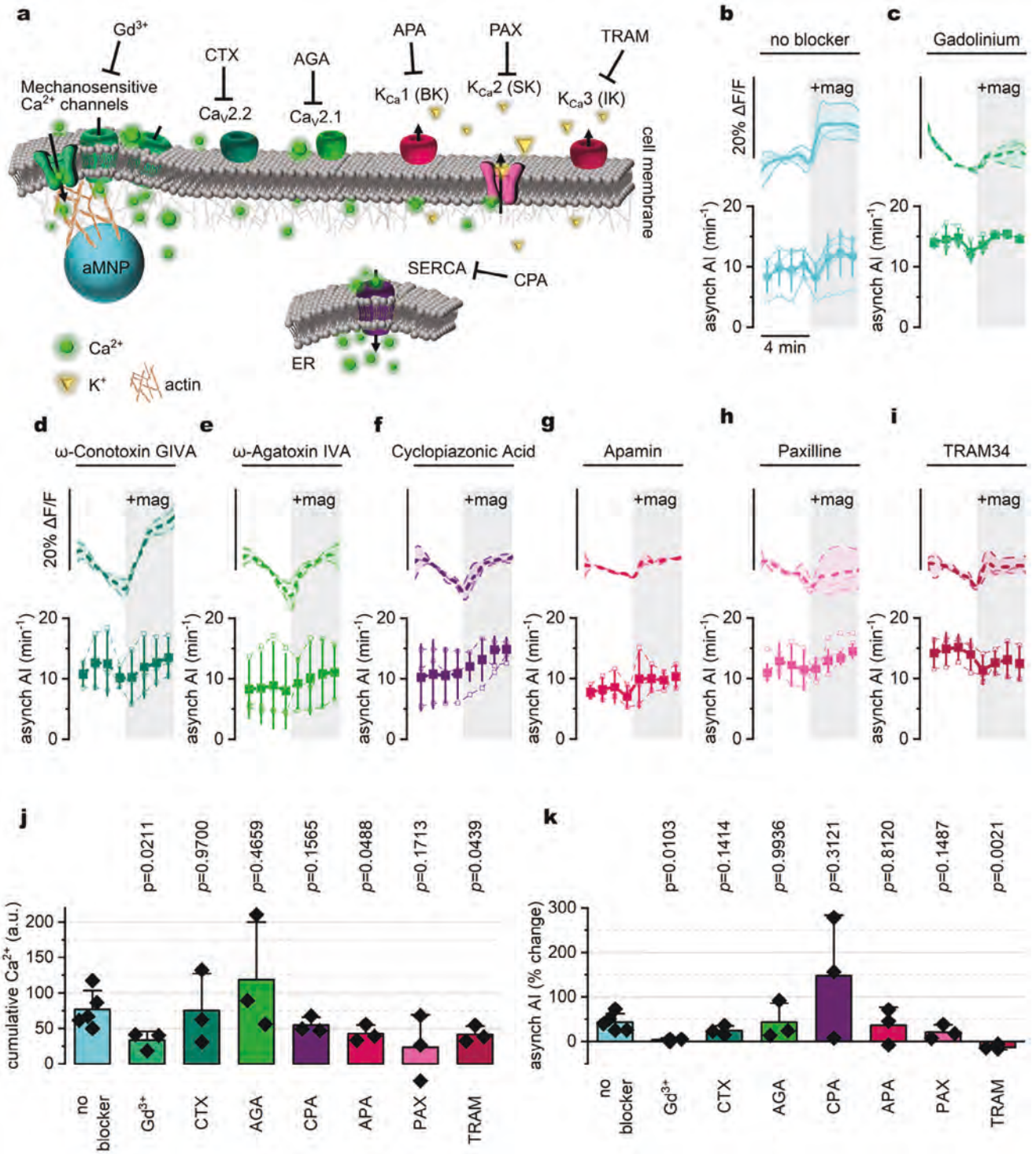

Figure 7. Pharmacological inhibition of Ca^{2+}-associated ion channels. a) Schematic of neuronal mechanosensitive receptors, hypothesized interactions activated by iNMF, and strategies to block them. (b–i) Pharmacological inhibition of 24 h afMNP exposed 14 DIV cortical networks. Blockers were added 20 min before iNMF. Line plot refers to resting Ca^{2+}, while line and symbol are the measured asynchronous activity index (AI). b iNMF controls with DMSO. c) Stretch-activated channel non-specific inhibitor gadolinium chloride (Gd^{3+}, 50 μM) d) N-type voltage-gated Ca^{2+} channel inhibitor ω-conotoxin GIVA (CTX, 100 nM). e) P/Q-type voltage-gated Ca^{2+} channel inhibitor ω-agatoxin IVA (AGA, 100 nM). f) SERCA pump inhibitor Cyclopiazonic Acid (CPA, 4 μM). g) SK, Ca^{2+} activated K channel inhibitor Apamin (APA, 100 nM). h) BK, Ca^{2+} activated K channel inhibitor Paxilline (PAX, 40 nM). i) IK, Ca^{2+} activated K channel inhibitor (TRAM34, 400 nM). j) Measured average Ca^{2+} influx (cumulative Ca^{2+}) and k) asynchronous activity responses to iNMF. Percent change is measured as the change from the final minute of iNMF to the first minute of activity. Bars are mean ± SD with n = 5 independent experiments for iNMF and n = 3 independent experiments for each blocker with iNMF (unpaired t-test of blocker against no blocker, two-tailed, p-values reported above the blocker).

The fluorescent and starch shells, along with the amine functionalization further shield the nanoparticle surface from the environment to reduce the interface for oxidation.[92] Combining these interactions, the delivered nanoparticle concentration can directly mediate the cytotoxicity, as increased concentration further increases the number of possible redox interactions. The cytotoxic effect of iron oxide nanoparticles is observed in neurons above 10 μg mL^{-1},[61,93,94] while we maintain a concentration of 2 μg mL^{-1}, further reducing the likelihood of cytotoxicity.

Previous work has shown that nanomagnetic forces induce Ca^{2+} influx independent of cell uptake.[22] Membrane-localized magnetic nanoparticles exhibit a force-dependent response, with reduced influx at forces below 100 pN.[21] In our experiments, a single afMNP could theoretically produce a maximum of 4 fN of magnetic gradient force, while a large cluster with a diameter of 300 nm exerts 0.2 pN. As these forces fall below the lower limit of 100 pN for force-mediated Ca^{2+}[21,62] we expect that afMNP internalization circumvents these constraints through cytosolic access. In cells containing multiple afMNPs, the application of the magnetic field causes the particles to migrate together, resulting in dipole-dipole forces dominating over magnetic gradient forces. Dipole-dipole forces from the chiMNPs at 100 nm separation generate up to 3.5 pN in single nanoparticles or 300 pN for clustered particles (Table S1, Supporting Information). Within the cell, the dense neuronal cytoskeleton can directly sense and propagate these internalized nanoparticle forces across the cell through complex links. In contrast, externally localized magnetic nanoparticles have a reduced capability to exert forces through dipole-dipole interactions. Magnetic nanoparticles adhered to the cell surface exert forces tangential to the cell membrane. Consequently, the particles may apply a local shear force to the extracellular matrix as they drag along the surface toward one another. The extracellular matrix binds to transmembrane receptors, such as integrins, providing mechanotransduction pathways into the cytosol. This cell-matrix interaction exhibits viscoelastic properties,[95] which dampen the magnitude of the force that particles exert while dragging along the surface. Neuronal mechanotransduction is functionally mediated by an assortment of membrane-bound MS channels tied to the actin cytoskeleton,[96,97] permitting intracellular force induction directly on the membrane and indirectly through cytoskeleton propagated forces. The complex link between the cytoskeleton-membrane anchoring is fundamental to mechanosensing and differentiation, where the interface may play a role in differentiating mechanical cues.[98] While the combined evidence suggests neuronal differentiation of localized forces intracellular and extracellular, the non-specific limitations of our technology prohibit conclusive evidence. Thus, future technologies should prioritize differentiating between the location of force generation to clarify the role and mechanisms associated with cell response to forces. Employing traction force measurements through nanopillar arrays[99,100] or deformation from scanning ion conductance microscopy[101,102] could provide the sensitivity necessary to differentiate the neuronal response relative to the location of nanoparticle-mediated forces. Understanding these mechanisms could provide crucial insights into the biophysics driving neuronal computation paradigms.

Primary dissociated cortical neuron cultures allowed us to investigate network-driven activity in detail without the indirect high-order inputs observed in vivo. Following Kasuba et al.'s recent electrophysiological observations of compression rate distinction under AFM,[18] we find iNMF acts as a slow mechanical deformation permitting a sustained Ca^{2+} influx to adjust the native excitability of neurons. The increased activity rate during the initial network response to iNMF matches similar observations to other magnetic nanoparticle forces.[2,21,22] Given imaging constraints, we could not differentiate between mechanically evoked Ca^{2+} influx and network-propagated responses. However, evidence suggests that both methods interact to activate neurons in the network.[4] The late-stage depression in Ca^{2+} event rate activity, which arises from shifts in the network state, could be attributed to short-term energetic effects[64] or a shift in circuit function. If the latter is true, this desynchronization response to iNMF could suggest a mechanically driven, Ca^{2+}-dependent alteration in neuronal potentiation and depression that presents with lasting shifts in network function. Given the relationship between cytosolic Ca^{2+} and cytoskeletal restructuring in the perspective of plasticity,[103–106] future work should prioritize understanding the mechanisms that cause desynchronization under force modulation to elucidate the interactions between forces, Ca^{2+} influx, and circuit-level dynamics. These observations might provide further insight into disease models such as subthreshold traumatic brain injuries. In in vitro models of stretch-mediated mechanical trauma, cortical networks exhibit similar network desynchronization of Ca^{2+} events driven by a shift in the excitatory tone of the network.[31] Mechanical stretch is further correlated with Ca^{2+} release from intracellular stores,[81,82] causing lasting shifts in neuronal activity.[79] Our observations of phasic asynchronization during iNMF on networks with Ca^{2+}-depleted ER stores and the lasting shifts during repeated iNMF suggest an overlap of the biophysical mechanisms.

Additionally, we exposed major biophysical components of iNMF-driven Ca^{2+} influx and activity modulation. Following previous observations of mechanical stimulation on primary neurons,[5,6] intracellular Ca^{2+} accumulates through the activation of MS channels. The slow and continuous Ca^{2+} influx over minutes suggests iNMF does not trigger rapid membrane depolarization, attributed to the activation of Ca^{2+}-sensitive sodium channels such as TRPM4 observed in the transient response to mechanical stimuli.[5] Instead, the cell may respond to the slow Ca^{2+} influx by activating BK and IK channels to restabilize the membrane potential, mitigating the evoked response and shifting the excitability of neurons.[107–109] We further this claim by highlighting that inhibiting N-type and P/Q-type voltage-gated Ca^{2+} channels did not alter the neuronal response. Voltage activation would trigger rapid Ca^{2+} influx by voltage-gated Ca^{2+} channels, contributing to the total influx of Ca^{2+}. Therefore, we suggest that slow and low-force iNMF stimulation does not polarize the neuron but alters excitability through MS channel activation. These studies could be extended in the future by using CRISPR knockouts or in vivo knockouts of specific ion channels to elucidate the biochemical mechanosensitive pathway.

Further questions remain open for future studies based on our observations. While our data suggest low force differences between internal and external mediated particle responses in neurons, it would be interesting to investigate this from a magnetic torque perspective.[43] Since the torque control of magnetic nanodiscs can be precisely regulated by tuning the

magnetic field strength, this low pN force regime could be interrogated to elucidate the neuronal and circuit-wide response. Our results present the ability to study parallel point source mechanical forces over the mm scale. Expanding the role of iNMF in complex circuits with high-order functions could provide further insight into neural computation during parallel mechanical stimulation. Alternatively, cell-specific nanoparticle targeting could mediate circuits through excitatory or inhibitory neuron stimulation. The large-scale assay can be further applied to prioritize force-mediated axon guidance by increasing force exposure.[110–112] Existing nerve repair and regeneration techniques employ nanotransducers to promote neurite growth via chemical,[113,114] thermal,[115] and mechanical[116,117] stimulation. Investigating low pN forces within the framework of nerve guidance and regeneration, alongside the relationship between Ca^{2+} dynamics and the cytoskeleton,[118] would be beneficial for understanding regrowth mechanisms. Finally, expanding this technology to other cell types, such as osteocytes or cardiomyocytes, could open new avenues for understanding cellular mechanics across the human body. This work shows the potential of iNMF to mechanically stimulate cortical networks, causing a lasting and repeatable shift in network state. As a tool, this further expands the mechano-modulation and neuro-modulation toolboxes for stimulation through endogenous mechanisms. Comprehending the role of this mechanical modulation in neuronal circuit dynamics could offer essential insights into the biophysics of neuronal computation paradigms and pave the way for future understandings of neurological disorders.

4. Experimental Section

Primary Cortical Neuron Culture: To monitor Ca^{2+} communication in mature neuronal networks, dissociated primary cortical neurons were grown from rat embryonic brain tissues (E18, TransnetYX). Neuronal cell cultures were established by following previously reported protocols by the authors.[57,63] In brief, cortical hemispheres were dissected from whole tissues in phosphate buffered solution (PBS) with 33 mM glucose (1% (v/v) penicillin-streptomycin) and dissociated using 10% (v/v) papain (Carica papaya, Roche, pH 7.3, 15 min, 37 °C). The dissociated cells were centrifuged (6 min, 500 rpm, at room temperature) and seeded into Petri dishes at a cell concentration of 1×10^6 cells mL^{-1}. Petri dishes had been coated with 0.05 mg mL^{-1} poly-d-lysine for at least 2 h and were washed 3× with PBS. High-density networks were plated at the highest concentration dropwise, with 10 min incubation at room temperature before adding culture growth media (96% Neurobasal Plus, 2% B27 Plus, 1% Glutamax, % is v/v) while all other cultures had the cell concentration suspended in 2 mL culture growth media before adding to the Petri Dish. Subsequently, neuronal cell cultures were incubated (37 °C, 95% air, 5% CO_2, Relative Humidity) for two weeks, and culture media (96% Neurobasal Plus, 2% (v/v) B27 Plus, 1% (v/v) PenStrep, 1% (v/v) Glutamax) was exchanged every three days.

Ca^{2+} Fluorometry During iNMF: To transduce magnetic gradients into mechanical forces, 100-nm starch-coated, amine-terminated, bionized nanoferrite fluorescent superparamagnetic nanoparticles (BNF-starch-far redF surface: amine, Micromod) were sonicated (37 kHz) for 30 min at 40 °C in culture media loaded to the cells at 10^{12} particles per mL(2 µg solid content/mL) and incubated for 24 h at 13 DIV. Before preparing for fluorescent imaging, cells were gently washed 3× with culture media to remove excess afMNPs. For magnetic nanoparticle surface chemistry contrasting experiments, three particles were used: Starch: 100-nm starch coated, bionized nanoferrite fluorescent superparamagnetic nanoparticles (BNF-Starch-far redF surface: NH2, Micromod), Anionic: 100-nm anionic charged magnetite fluorescent superparamagnetic nanoparticles (nano-screenMAG UC/A, Chemicell) and neutral: 100-nm cationic charged magnetite fluorescent superparamagnetic nanoparticles (nano-screenMAG-UC/C, Chemicell). The manufacturer-specified cationic magnetite nanoparticles were found to present a neutral surface charge (Figure 4b); therefore, they were labeled as neutral within the text. Magnetic nanoparticles were characterized for zeta potential and radius were found using a dynamic light scattering analyzer (Mobius, Wyatt Technology). Particles were incubated with the cells for either 4 or 24 h before cell wash and Fluo-4 AM incubation. Ca^{2+} signaling was recorded through conventional fluorescent dye imaging methods. In short, Fluo-4 AM with probenecid acid (Thermo) was loaded into the cells (1:1 v/v) and incubated for 60 min (37 °C, 95% air, 5% CO_2). Following incubation, the cells were gently washed 3x with culture media and incubated for 30 min. Ca^{2+} dye-loaded live neuronal cultures were monitored using wide-field imaging with an inverted fluorescent microscope (Leica DMI-8, 10×) at (37 °C, 95% air, 5% CO_2) using a manual gas mixed stage top incubator (Okolab). Fluorescent videos were recorded for 960 frames at 4 Hz with 240 ms exposure. A baseline video was recorded, and immediately following the final frame, the magnetic device was lowered onto the Petri dish, and a modulation recording was started. Similarly, when the final frame for modulation was recorded, the magnetic device was removed, and a recovery recording was started. A sham (non-magnetic) device was added to the samples for control sets.

Pharmacological Treatments: For endocytosis experiments, pharmacological treatments of Pitstop 2 (Sigma, final conc. 20 µM) and cytochalasin D (Thermo, final conc. 1 µM) were prepared in culture media at 37 °C and added 30 min before afMNPs. Neurons were continuously exposed to the treatments with the afMNPs for 24 h before 3X cell wash, incubated for 1 h, and then incubated with Fluo-4AM (1:1 v/v) for 1 h. Before imaging, the cells were gently washed 3x with culture media. Further channel blockers and peptide inhibitors were prepared in culture media (37 °C) and incubated for 20 min with the cells before imaging. Stretch-activated Ca^{2+} channels were non-specifically blocked with Gadolinium Chloride (Gd^{3+}, Sigma Aldrich, final conc. 50 µM). Voltage-gated Ca^{2+} channels N-type and P/Q type were blocked with ω-conotoxin GIVA (CTX, Alomone, final conc. 100 nM) and ω-agatoxin IVA (AGA, Alomone, final conc. 100 nM) respectively. The SERCA pump was blocked with Cyclopiazonic Acid (CPA, Alomone, 4 µM). The large conductance (BK), small conductance (SK), and intermediate conductance (IK) Ca^{2+} associated potassium channels were blocked with Paxilline (PAX, Alomone,40 nM), Apamin (APA, Alomone, 100 nM) and TRAM34 (Alomone, 400 nM) respectively. To induce high-activity networks, bicuculline (Alomone, final conc. 100 µM) was added after the 5 min post-iNMF recording to permit 15 min incubation (37 °C) before continuing recording.

Video Processing: A detailed description is provided along with Figure S7 (Supporting Information) and the corresponding Supporting Information section: Image processing pipeline to obtain temporal Ca^{2+} dynamics. In brief, Ca^{2+} videos (´.lif´) were imported into ImageJ. The soma of neurons presenting Ca^{2+} were segmented from the videos using the oval selection tool and ROI manager. A minimum of 200 and a maximum of 2000 neurons were selected from each sample. Each video was stabilized using Template matching,[119] and slight shifts (±10 µm) from the addition and removal of the magnetic field were adjusted by batch translating the [x,y] coordinates of the ROIs to match visually. The mean intensity was exported (´.csv´) for each video with the ROIs translated. Each signal (F) was imported into MATLAB 2023a, and an initial lower envelope (LE) was fit over the complete recording period with a peak separation of 10 s to approximate the Ca^{2+} intensity sans influx events. The signal's baseline intensity (F_0) was estimated as the mean of the lower envelope during the baseline period and used to generate a normalized signal: $\Delta F/F = (F-F_0)/F_0$ and resting Ca^{2+} waveform: resting $Ca^{2+} = (LE-F_0)/F_0$ The cumulative Ca^{2+} influx was then computed as the area under the resting Ca^{2+} curve, with the y = 0 starting at the resting Ca^{2+} cumulative influx during the modulation period of the video. For Ca^{2+} event detection, peaks were identified from $\Delta F/F$ using the findpeaks function with a minimum peak width of two frames and a minimum peak prominence of two standard

deviations of the baseline ΔF/F signal. The Sørenson-dice correlation was computed pairwise between Ca^{2+} event trains, where two inactive cells indicated no correlation (e.g., 0). Synchronous Ca^{2+} event rates were detected as influx events from >10% of the cell population, while all other periods were classified as asynchronous.

Statistical Analysis: All data comparisons were tested for normality with the Shapiro–Wilk test. Normally distributed data was analyzed with parametric tests and non-normally distributed data compared with Mann–Whitney tests, with data reported in the text as mean ± standard deviation. Data collection and analysis were not performed blind to the experimental conditions. All software for video signal processing techniques are detailed in the Section S6 (Supporting Information). Statistical significance was evaluated at $p \leq 0.05$. Data was not outlier-filtered. Sample count, statistical tests, and *p*-values are detailed in figure captions. Bar plots are reported with bar at mean and error bar as standard deviation if not specified. Symbols indicating statistical significance within figures are: n.s.: $p > 0.05$, *: $0.01 < p \leq 0.05$, **: $0.001 < p \leq 0.01$, ***: $0.0001 < p \leq 0.001$, ****: $p \leq 0.0001$ and detailed within figure captions.

Supporting Information

Supporting Information is available from the Wiley Online Library or from the author.

Acknowledgements

The authors thank Mackenna Landis for performing dissociation and Zeynep Malkoc for performing dissociation and aid in zeta potential analysis. This work was supported by the NSF Grant #CBET-1846271 (CAREER award, AK) and by the National Institute of General Medical Sciences of the National Institutes of Health under Award Number P20GM103474 (INBRE, CB). The content is solely the responsibility of the author.

Conflict of Interest

AK, CB and CK would like to declare inventorship on a provisional patent application associated with this research study filed by Montana State University (US 63/446,770 (Prov #2), filed February 17th, 2023). AK and CB are co-founders and have stock and ownership interests in NanoMagnetic Solutions, Inc. No financial support was received from NanoMagnetic Solutions, Inc. for the purpose of this research study.

Author Contributions

CB designed and performed all experiments. AK conceptualized, designed, and supervised the study. Both authors wrote and revised the manuscript.

Data Availability Statement

The data that support the findings of this study are available from the corresponding author upon reasonable request.

Keywords

calcium, magnetic nanoparticles, mechanical stimulation, neuromodulation, neuronal networks

Received: August 14, 2024
Revised: October 14, 2024
Published online: October 26, 2024

[1] W. J. Tyler, *Nat. Rev. Neurosci.* **2012**, *13*, 867.
[2] D. Gregurec, A. W. Senko, A. Chuvilin, P. D. Reddy, A. Sankararaman, D. Rosenfeld, P. H. Chiang, F. Garcia, I. Tafel, G. Varnavides, E. Ciocan, P. Anikeeva, *ACS Nano* **2020**, *14*, 8036.
[3] B. M. Gaub, D. J. Müller, *Nano Lett.* **2017**, *17*, 2064.
[4] B. Cepkenovic, F. Friedland, E. Noetzel, V. Maybeck, A. Offenhäusser, *Sci. Rep.* **2023**, *13*, 20669.
[5] S. Yoo, D. R. Mittelstein, R. C. Hurt, J. Lacroix, M. G. Shapiro, *Nat. Commun.* **2022**, *13*, 493.
[6] B. M. Gaub, K. C. Kasuba, E. Mace, T. Strittmatter, P. R. Laskowski, S. A. Geissler, A. Hierlemann, M. Fussenegger, B. Roska, D. J. Müller, *Proc. Natl. Acad. Sci. USA* **2019**, *117*, 848.
[7] Z. Qiu, J. Guo, S. Kala, J. Zhu, Q. Xian, W. Qiu, G. Li, T. Zhu, L. Meng, R. Zhang, H. C. Chan, H. Zheng, L. Sun, *iScience* **2019**, *21*, 448.
[8] C. H. Coles, F. Bradke, *Curr. Biol.* **2015**, *25*, 677.
[9] L. He, R. Kooistra, R. Das, E. Oudejans, E. van Leen, J. Ziegler, S. Portegies, B. de Haan, A. V. R. Altena, R. Stucchi, A. F. M. Altelaar, S. Wieser, M. Krieg, C. C. Hoogenraad, M. Harterink, *Elife* **2020**, *9*, e55111.
[10] A. Falconieri, S. De Vincentiis, V. Cappello, D. Convertino, R. Das, S. Ghignoli, S. Figoli, S. Luin, F. Català-Castro, L. Marchetti, U. Borello, M. Krieg, V. Raffa, *Cell Rep.* **2023**, *42*, 111912.
[11] K. C. Flynn, *Bioarchitecture* **2013**, *3*, 86.
[12] M. Maekawa, T. Ishizaki, S. Boku, N. Watanabe, A. Fujita, A. Iwamatsu, T. Obinata, K. Ohashi, K. Mizuno, S. Narumiya, *Science* **1999**, *285*, 895.
[13] Y. Sekino, N. Kojima, T. Shirao, *Neurochem. Int.* **2007**, *51*, 92.
[14] P. Hotulainen, O. Llano, S. Smirnov, K. Tanhuanpää, J. Faix, C. Rivera, P. Lappalainen, *J. Cell Biol.* **2009**, *185*, 323.
[15] H. Ucar, S. Watanabe, J. Noguchi, Y. Morimoto, Y. Iino, S. Yagishita, N. Takahashi, H. Kasai, *Nature* **2021**, *600*, 686.
[16] L. Jammal Salameh, S. H. Bitzenhofer, I. L. Hanganu-Opatz, M. Dutschmann, V. Egger, *Science* **2024**, *383*, eadk8511.
[17] M. Joy, D. L. Nall, B. Emon, K. Lee, A. Barishman, M. Ahmed, S. Rahman, P. R. Selvin, M. T. A. Saif, *Proc. Natl. Acad. Sci. USA* **2023**, *120*, e2311995120.
[18] K. Kasuba, A. Buccino, J. Bartram, B. M. Gaub, F. J. Fauser, S. Ronchi, S. Kumar, S. Geissler, M. M. Nava, A. Hierlemann, D. J. Müller, *Nat. Nanotechnol.* **2024**, *19*, 825.
[19] Y. A. Nikolaev, P. J. Dosen, D. R. Laver, D. F. Van Helden, O. P. Hamill, *Brain Res.* **2015**, *1608*, 1.
[20] Y. Tufail, A. Matyushov, N. Baldwin, M. L. Tauchmann, J. Georges, A. Yoshihiro, S. I. H. Tillery, W. J. Tyler, *Neuron* **2010**, *66*, P681.
[21] A. Tay, D. Di Carlo, *Nano Lett.* **2017**, *17*, 886.
[22] A. Tay, A. Kunze, C. Murray, D. Di Carlo, *ACS Nano* **2016**, *10*, 2331.
[23] M. Brini, T. Calì, D. Ottolini, E. Carafoli, *Cell. Mol. Life Sci.* **2014**, *71*, 2787.
[24] G. T. Charras, B. A. Williams, S. M. Sims, M. A. Horton, *Biophys. J.* **2004**, *87*, 2870.
[25] H. Cho, J. Shin, C. Shin, S.-Y. Lee, U. Oh, *J. Neurosci.* **2002**, *22*, 1238.
[26] T. Grevesse, B. E. Dabiri, K. Parker, S. Gabriele, *Sci. Rep.* **2015**, *5*, 9475.
[27] S. K. Rastogi, R. Garg, M. Scopelliti, B. I. Pinto, J. E. Hartung, S. Kim, C. G. E. Murphey, N. Johnson, D. San Roman, F. Bezanilla, J. F. Cahoon, M. S. Gold, M. Chamanzar, T. Cohen-Karni, *Proc. Natl. Acad. Sci. USA* **2020**, *117*, 13339.
[28] M. A. Rabadan, E. De La Cruz, S. B. Rao, Y. Chen, C. Gong, G. Crabtree, B. Xu, S. Markx, J. A. Gogos, R. Yuste, R. Tomer, *Nat. Commun.* **2022**, *13*, 3340.
[29] R. Yuste, R. Cossart, E. Yaksi, *Neuron* **2024**, *112*, 875.
[30] M. Saponati, M. Vinck, *Nat. Commun.* **2023**, *14*, 4985.
[31] T. P. Patel, S. C. Ventre, D. F. Meaney, *Ann. Biomed. Eng.* **2012**, *40*, 23.

[32] P. B. Goforth, J. Ren, B. S. Schwartz, L. S. Satin, *J. Neurophysiol.* **2011**, *105*, 2350.
[33] M. C. LaPlaca, G. R. Prado, D. K. Cullen, H. R. Irons, *Int. Conf. of the IEEE Engineering in Medicine and Biology Society*, IEEE, New York **2006**.
[34] M. Liu, W. Song, P. Li, Y. Huang, X. Gong, G. Zhou, X. Jia, L. Zheng, Y. Fan, *PLoS One* **2013**, *8*, e63473.
[35] P. P. Ye, J. R. Brown, K. B. Pauly, *Ultrasound Med. Biol.* **2016**, *42*, 1512.
[36] S. S. Yoo, A. Bystritsky, J. H. Lee, Y. Zhang, K. Fischer, B. K. Min, N. J. McDannold, A. Pascual-Leone, F. A. Jolesz, *Neuroimage* **2011**, *56*, 1267.
[37] W. Lee, H. Kim, Y. Jung, I. U. Song, Y. A. Chung, S. S. Yoo, *Sci. Rep.* **2015**, *5*, 8743.
[38] S. Sharabi, D. Daniels, D. Last, D. Guez, Z. Zivli, D. Castel, Y. Levy, A. Volovick, J. Grinfeld, I. Rachmilevich, T. Amar, Y. Mardor, S. Harnof, *Brain Stimul.* **2019**, *12*, 1.
[39] B. U. Hoffman, Y. Baba, S. A. Lee, C.-K. Tong, E. E. Konofagou, E. A. Lumpkin, *Proc. Natl. Acad. Sci. USA* **2022**, *119*, e2115821119.
[40] H. T. McMahon, E. Boucrot, *J. Cell Sci.* **2015**, *128*, 1065.
[41] W. Wei, Z. Wang, *J. Nanomater.* **2018**, *2018*, 6246917.
[42] C. Collier, N. Muzzio, R. Thevi Guntnur, A. Gomez, C. Redondo, R. Zurbano, I. K. Schuller, C. Monton, R. Morales, G. Romero, *Adv. Healthcare Mater.* **2022**, *11*, 2101826.
[43] A. Gomez, N. Muzzio, A. Dudek, A. Santi, C. Redondo, R. Zurbano, R. Morales, G. Romero, *Cell Mol. Bioeng.* **2023**, *16*, 283.
[44] R. Munshi, S. M. Qadri, A. Pralle, *Front. Neurosci.* **2018**, *12*.
[45] R. Chen, G. Romero, M. G. Christiansen, A. Mohr, P. Anikeeva, *Science* **2015**, *347*, 1477.
[46] D. Rosenfeld, A. W. Senko, J. Moon, I. Yick, G. Varnavides, D. Gregureć, F. Koehler, P.-H. Chiang, M. G. Christiansen, L. Y. Maeng, A. S. Widge, P. Anikeeva, *Sci. Adv.* **2020**, *6*, eaaz3734.
[47] C. Sebesta, D. T. Hinojosa, B. Wang, J. Asfouri, Z. Li, G. Duret, K. Jiang, Z. Xiao, L. Zhang, Q. Zhang, V. L. Colvin, S. M. Goetz, A. V. Peterchev, H. A. Dierick, G. Bao, J. T. Robinson, *Nat. Mater.* **2022**, *21*, 951.
[48] J. uk Lee, W. Shin, Y. Lim, J. Kim, W. R. Kim, H. Kim, J. H. Lee, J. Cheon, *Nat. Mater.* **2021**, *20*, 1029.
[49] S.-H. Choi, J. Shin, C. Park, J. Lee, J. Lee, Y. Ambo, W. Shin, R. Yu, J.-Y. Kim, J. Lah, D. Shin, G. Kim, K. Noh, W. Koh, C. J. Lee, J.-H. Lee, M. Kwak, J. Cheon, *Nat. Nanotechnol.* **2024**, *19*, 1333.
[50] G. Romero, J. Park, F. Koehler, A. Pralle, P. Anikeeva, *Nat. Rev. Methods Primers* **2022**, *2*, 92.
[51] S. A. Hescham, P. H. Chiang, D. Gregurec, J. Moon, M. G. Christiansen, A. Jahanshahi, H. Liu, D. Rosenfeld, A. Pralle, P. Anikeeva, Y. Temel, *Nat. Commun.* **2021**, *12*, 5569.
[52] M. G. Christiansen, A. W. Senko, P. Anikeeva, *Annu. Rev. Neurosci.* **2019**, *42*, 271.
[53] V. Zablotskii, T. Polyakova, O. Lunov, A. Dejneka, *Sci. Rep.* **2016**, *6*, 37407.
[54] S. S. Shevkoplyas, A. C. Siegel, R. M. Westervelt, M. G. Prentiss, G. M. Whitesides, *Lab Chip* **2007**, *7*, 1294.
[55] M. Yuan, E. A. Bancroft, J. Chen, R. Srinivasan, Y. Wang, *ACS Appl. Nano Mater.* **2022**, *5*, 205.
[56] A. Kunze, C. T. Murray, C. Godzich, J. Lin, K. Owsley, A. Tay, D. Di Carlo, *Lab Chip* **2017**, *17*, 842.
[57] A. Kunze, P. Tseng, C. Godzich, C. Murray, A. Caputo, F. E. Schweizer, D. Di Carlo, *ACS Nano* **2015**, *9*, 3664.
[58] X. Jiang, J. Dausend, M. Hafner, A. Musyanovych, C. Röcker, K. Landfester, V. Mailänder, G. U. Nienhaus, *Biomacromolecules* **2010**, *11*, 748.
[59] D. Burnand, A. Milosevic, S. Balog, M. Spuch-Calvar, B. Rothen-Rutishauser, J. Dengjel, C. Kinnear, T. L. Moore, A. Petri-Fink, D. Burnand, A. Petri-Fink, A. Milosevic, S. Balog, M. Spuch-Calvar, B. Rothen-Rutishauser, T. L. Moore, J. Dengjel, C. Kinnear, *Small* **2018**, *14*, 1613.
[60] S. Behzadi, V. Serpooshan, W. Tao, M. A. Hamaly, M. Y. Alkawareek, E. C. Dreaden, D. Brown, A. M. Alkilany, O. C. Farokhzad, M. Mahmoudi, *Chem. Soc. Rev.* **2017**, *46*, 4218.
[61] Z. Sun, V. Yathindranath, M. Worden, J. A. Thliveris, S. Chu, F. E. Parkinson, T. Hegmann, D. W. Miller, *Int. J. Nanomed.* **2013**, *8*, 961.
[62] M. Meister, *Elife* **2016**, *5*, e17210.
[63] C. L. Beck, C. J. Hickman, A. Kunze, *Sci. Rep.* **2020**, *10*, 12568.
[64] R. Sattler, M. Tymianski, *J. Mol. Med.* **2000**, *78*, 3.
[65] M. J. Berridge, M. D. Bootman, P. Lipp, *Nature* **1998**, *395*, 645.
[66] P. Foroozandeh, A. A. Aziz, *Nanoscale Res. Lett.* **2018**, *13*, 339.
[67] P. Forscher, S. J. Smith, *J. Cell Biol.* **1988**, *107*, 1505.
[68] I. Foissner, G. O. Wasteneys, *Protoplasma* **2000**, *214*, 33.
[69] D. Dutta, C. D. Williamson, N. B. Cole, J. G. Donaldson, *PLoS One* **2012**, *7*, e45799.
[70] I. Foissner, G. O. Wasteneys, *Plant Cell Physiol.* **2007**, *48*, 585.
[71] P. Rees, J. W. Wills, M. R. Brown, C. M. Barnes, H. D. Summers, *Nat. Commun.* **2019**, *10*, 2341.
[72] M. Ivenshitz, M. Segal, *J. Neurophysiol.* **2010**, *104*, 1052.
[73] D. A. Wagenaar, J. Pine, S. M. Potter, *BMC Neurosci.* **2006**, *7*, 11.
[74] Y. A. Ermakov, K. Kamaraju, K. Sengupta, S. Sukharev, *Biophys. J.* **2010**, *98*, 1018.
[75] P. Chanana, A. Uosef, N. Vaughn, M. Suarez-Villagran, R. M. Ghobrial, M. Kloc, J. Wosik, *Cells* **2022**, *11*, 757.
[76] R. A. Caldwell, H. F. Clemo, C. M. Baumgarten, *Am. J. Physiol. Cell Physiol.* **1998**, *275*, C619.
[77] L. M. Boland, T. A. Brown, R. Dingledine, *Brain Res.* **1991**, *563*, 142.
[78] D. Bleakman, D. Bowman, C. P. Bath, P. F. Brust, E. C. Johnson, C. R. Deal, R. J. Miller, S. B. Ellis, M. M. Harpold, M. Hans, C. J. Grantham, *Neuropharmacology* **1995**, *34*, 753.
[79] J. T. Weber, B. A. Rzigalinski, E. F. Ellis, *J. Biol. Chem.* **2001**, *276*, 1800.
[80] J. T. Weber, B. A. Rzigalinski, K. A. Willoughby, S. F. Moore, E. F. Ellis, *Cell Calcium* **1999**, *26*, 289.
[81] J. A. Staal, T. C. Dickson, R. Gasperini, Y. Liu, L. Foa, J. C. Vickers, *J. Neurochem.* **2010**, *112*, 1147.
[82] B. T. Jacques-Fricke, Y. Seow, P. A. Gottlieb, F. Sachs, T. M. Gomez, *J. Neurosci.* **2006**, *26*, 5656.
[83] S. H. Lee, K. H. Bae, S. H. Kim, K. R. Lee, T. G. Park, *Int. J. Pharm.* **2008**, *364*, 94.
[84] C. W. Evans, M. Fitzgerald, T. D. Clemons, M. J. House, B. S. Padman, J. A. Shaw, M. Saunders, A. R. Harvey, B. Zdyrko, I. Luzinov, G. A. Silva, S. A. Dunlop, K. S. Iyer, *ACS Nano* **2011**, *5*, 8640.
[85] A. Chakraborty, N. R. Jana, *J. Phys. Chem. Lett.* **2015**, *6*, 3688.
[86] Y. Portilla, Y. Fernández-Afonso, S. Pérez-Yagüe, V. Mulens-Arias, M. P. Morales, L. Gutiérrez, D. F. Barber, *J. Nanobiotechnol.* **2022**, *20*, 543.
[87] M. Sousa de Almeida, E. Susnik, B. Drasler, P. Taladriz-Blanco, A. Petri-Fink, B. Rothen-Rutishauser, *Chem. Soc. Rev.* **2021**, *50*, 5397.
[88] R. Agarwal, S. Adhikary, S. Bhattacharya, S. Goswami, D. Roy, S. Dutta, A. Ganguly, S. Nanda, P. Rajak, *Environ. Sci.: Advances* **2024**, *3*, 635.
[89] Z. Yu, Q. Li, J. Wang, Y. Yu, Y. Wang, Q. Zhou, P. Li, *Nanoscale Res. Lett.* **2020**, *15*, 115.
[90] T. R. Pisanic, J. D. Blackwell, V. I. Shubayev, R. R. Fiñones, S. Jin, *Biomaterials* **2007**, *28*, 2572.
[91] J. Wu, T. Ding, J. Sun, *Neurotoxicology* **2013**, *34*, 243.
[92] C. J. Rivet, Y. Yuan, D.-A. Borca-Tasciuc, R. J. Gilbert, *Chem. Res. Toxicol.* **2011**, *25*, 153.
[93] R. P. Badman, S. L. Moore, J. L. Killian, T. Feng, T. A. Cleland, F. Hu, M. D. Wang, *Sci. Rep.* **2020**, *10*, 11239.
[94] J. A. Kim, N. Lee, B. H. Kim, W. J. Rhee, S. Yoon, T. Hyeon, T. H. Park, *Biomaterials* **2011**, *32*, 2871.

[95] O. Chaudhuri, J. Cooper-White, P. A. Janmey, D. J. Mooney, V. B. Shenoy, *Nature* **2020**, *584*, 535.
[96] S. Sasaki, N. Yui, Y. Noda, *Biochim. Biophys. Acta (BBA) – Biomembranes* **2014**, *1838*, 514.
[97] E. A. Morachevskaya, A. V. Sudarikova, *Am. J. Physiol. Cell Physiol.* **2021**, *320*, C696.
[98] B. T. Goult, J. Yan, M. A. Schwartz, *J. Cell Biol.* **2018**, *217*, 3776.
[99] D. Yu, Q. Nie, J. Xue, R. Luo, S. Xie, S. Chao, E. Wang, L. Xu, Y. Shan, Z. Liu, Y. Li, Z. Li, *Adv. Healthcare Mater.* **2023**, *12*, 2301126.
[100] Y. Jin, Y. Zhang, H. Ouyang, M. Peng, J. Zhai, Z. Li, *Sens. Mater.* **2015**, *27*, 1071.
[101] A. Gesper, D. Thatenhorst, S. Wiese, T. Tsai, I. D. Dietzel, P. Happel, *Scanning* **2015**, *37*, 226.
[102] A. Tanaka, R. Tanaka, N. Kasai, S. Tsukada, T. Okajima, K. Sumitomo, *J. Struct. Biol.* **2015**, *191*, 32.
[103] C. Rosenmund, G. L. Westbrook, *Neuron* **1993**, *10*, 805.
[104] K. Furukawa, W. Fu, Y. Li, W. Witke, D. J. Kwiatkowski, M. P. Mattson, *J. Neurosci.* **1997**, *17*, 8178.
[105] T. Saneyoshi, Y. Hayashi, *Cytoskeleton* **2012**, *69*, 545.
[106] G. Chindemi, M. Abdellah, O. Amsalem, R. Benavides-Piccione, V. Delattre, M. Doron, A. Ecker, A. T. Jaquier, J. King, P. Kumbhar, C. Monney, R. Perin, C. Rössert, A. M. Tuncel, W. Van Geit, J. DeFelipe, M. Graupner, I. Segev, H. Markram, E. B. Muller, *Nat. Commun.* **2022**, *13*, 3038.
[107] Z. Niday, B. P. Bean, *J. Neurosci.* **2021**, *41*, 2854.
[108] J. J. Sheehan, B. L. Benedetti, A. L. Barth, *Epilepsia* **2024**, *65*,711.
[109] M. V. Roshchin, V. N. Ierusalimsky, P. M. Balaban, E. S. Nikitin, *Sci. Rep.* **2020**, *10*, 14484.
[110] K. Baba, W. Yoshida, M. Toriyama, T. Shimada, C. F. Manning, M. Saito, K. Kohno, J. S. Trimmer, R. Watanabe, N. Inagaki, *Elife* **2018**, *7*, e34593.
[111] E. K. Pillai, K. Franze, *Neuron* **2024**, *112*, 342.
[112] D. Bray, *Dev. Biol.* **1984**, *102*, 379.
[113] Y. Shan, L. Xu, X. Cui, E. Wang, F. Jiang, J. Li, H. Ouyang, T. Yin, H. Feng, D. Luo, Y. Zhang, Z. Li, *Mater. Horiz.* **2023**, *11*, 1032.
[114] Y. Yang, X. Yin, H. Wang, W. Qiu, L. Li, F. Li, Y. Shan, Z. Zhao, Z. Li, J. Guo, J. Zhang, Y. Zhao, *Nano Energy* **2023**, *107*, 108145.
[115] D. Rosenfeld, H. Field, Y. J. Kim, K. K. L. Pang, K. Nagao, F. Koehler, P. Anikeeva, *Adv. Funct. Mater.* **2022**, *32*, 0224558.
[116] S. De Vincentiis, A. Falconieri, V. Scribano, S. Ghignoli, V. Raffa, *Int. J. Mol. Sci.* **2020**, *21*, 8009.
[117] S. de Vincentiis, A. Falconieri, M. Mainardi, V. Cappello, V. Scribano, R. Bizzarri, B. Storti, L. Dente, M. Costa, V. Raffa, *J. Neurosci.* **2020**, *40*, 4997.
[118] R. J. Gasperini, M. Pavez, A. C. Thompson, C. B. Mitchell, H. Hardy, K. M. Young, J. K. Chilton, L. Foa, *Mol. Cell. Neurosci.* **2017**, *84*, 29.
[119] Q. Tseng, I. Wang, E. Duchemin-Pelletier, A. Azioune, N. Carpi, J. Gao, O. Filhol, M. Piel, M. Th, M. Balland, **2011**,*11*, 2231.